Recent trends in the wind-driven California Current Upwelling System

Y. Quilfen[1] , J. Shutler[2], J.-F. Piolle[1], E. Autret[1]

[1]IFREMER, Univ. Brest, CNRS, IRD, Laboratoire d'Océanographie Physique et Spatiale (LOPS), IUEM, Brest, France
[2]College of Life and Environmental Sciences, University of Exeter, Penryn, UK

Corresponding author: Yves Quilfen (Yves.Quilfen@ifremer.fr)

Highlights:

- The seasonal upwelling transport has increased by as much as 25% in 1996-2018
- Spatially structured trends in pH and Chl-a are observed for the same period
- Results from satellite analysis and model reanalysis products diverge locally

Abstract

Long-term changes in the marine ecosystems of the Eastern Boundary Upwelling Systems (EBUS) are predicted due to anthropogenic climate change. In particular, global ocean acidification is having a profound effect on the coastal waters of the EBUS, affecting the entire trophic chain, net primary production (NPP) and related economic activities such as fisheries. Another predicted change related to human activity is that of upwelling dynamics with expected long-term changes in upwelling winds as proposed by Bakun (1990), Bakun et al. (2015) and Rykaczewski et al. (2015). Although these predicted long-term changes may emerge only later in the 21st century, this has fueled many studies using historical data. Long-term increase in upwelling winds has thus been a much debated topic, showing that there is considerable uncertainty depending on the EBUS considered, the effect of natural climate fluctuations, the choice of wind dataset, the time period considered, and the methodologies and significance tests applied. Therefore, there is an immediate interest in being able to monitor upwelling using verified and self-consistent wind data sets. This work focused on a sensitivity study of the estimated trends in upwelling winds in the California Current Upwelling System (CCUS), for the most recent period 1996-2018, using the two state-of-the-art satellite wind analyses and two atmospheric model re-analyses. Embedded into the strong modulation by natural climate fluctuations on interannual and decadal time scales, we do see an increase in upwelling-favorable winds in the core of the CCUS, with a local increase of more than 25% in seasonal upwelling transport for the period considered. In this central upwelling zone, a good agreement on stronger equatorward winds for the winter and spring seasons is found between the different datasets, although with different significance levels. Conversely, conflicting results are found in the southernmost part of the CCUS between the satellite analyses and the model reanalyses. Systematic, time-dependent differences are found between the wind products,

highlighting the need to further investigate the poorly documented temporal stability of these widely used wind long-term climatology products. The observed spatial structuring of the estimated wind trends is consistent with the trend analysis of water chlorophyll-a, partial pressure of CO_2, and basity (pH) analysis products. This result is consistent with changes being important for modulating the carbonate system within the CCUS.

1. Introduction

EBUS are very active biogeochemical systems, which adapt to the timing and strength of upwelling winds whose natural variability extends over various spatial and temporal scales. Ecosystem productivity responds to this external forcing in complex ways, raising several unresolved questions and issues regarding the future of the coastal upwelling ecosystem and the global carbon cycle, as explained by Di Lorenzo (2015). Although there is past evidence that these upwelling ecosystems are resilient to natural changes in ocean-atmosphere dynamics such as those associated with El Niño events in the CCUS, there is great uncertainty about how these EBUS may respond to a long-term increase in the mean magnitude of upwelling winds and ocean stratification due to climate change (García-Reyes et al., 2015). Indeed, increased coastal upwelling in parts of the four eastern boundary upwelling systems has been predicted as a result of a deterministic and predictable increase in the contrast between atmospheric pressure over the ocean and land (Bakun, 1990), and/or as a result of a long-term poleward shift of ocean high pressure systems (Bakun et al., 2015; Rykaczewski et al., 2015). In addition, ocean acidification and deoxygenation are occurring within upwelling ecosystems (e.g. Feely et al., 2008; Gruber et al., 2012; Deutsch et al., 2020), likely driven by long-term global uptake of atmospheric CO_2 by the ocean. However, clearly it is essential to understand how long-term changes in upwelling winds, that draw up water with

distinctly different carbonate properties from depth, will also contribute to increased acidification and biogeochemical development of EBUS.

Numerous studies on trends in upwelling winds (e.g. Rykacewski and Checkley, 2008; Narayan et al., 2010; García-Reyes and Largier, 2010; Iles et al., 2012) followed the Bakun's (1990) article, fueled by the anticipated effects on coastal ecosystems and the global carbon cycle. Sydeman et al. (2014) conducted a meta-analysis of different past studies to discuss the consistency of the local long-term intensification of upwelling winds, and the contrasting results related to the choice of the period and duration studied, the effects of natural climate variability (interannual and lower frequency), the effects of seasonality, changes in instrumentation and the scarcity of spatially resolved observations, differences in the reporting of the statistical significance of trends, and differences in the results of model reanalyses and observations used. Furthermore, recent studies have identified that an increase in upwelling winds in a warming climate would be likely for only three of the EBUS (Wang et al., 2015), but not for the California upwelling, or that long-term changes in upwelling will emerge only late in the 21st century (Brady et al., 2017). Rykaczewski et al. (2015), using an ensemble of ocean-atmosphere coupled models, show the relationship between poleward migration of major ocean high pressure systems and changes in upwelling winds along the four EBUS, with spatial and temporal structuring of the predicted changes. Summer upwelling winds are predicted to intensify in the poleward area and weaken in the equatorward area, but with differing significant levels. Thus, they found equivocal results in the northern part of the CCUS and a significant decrease in upwelling winds in the southern part. While these modelling studies can cover very long time scales to provide results consistent with the scale of projected changes, there is also an immediate interest in continuously monitoring actual changes with newly developed or improved wind climatology. Indeed, former atmospheric model reanalyses used in many

116 upwelling trend studies may be affected by systematic biases (e.g. Belmonte and Stoffelen, 2019;
Taboada et al., 2019). In the present study, we intend to elaborate on this topic, addressing the
118 various issues related to the recent period and the CCUS, especially those dealing with data caveats,
which have been overlooked in most studies. Our approach is therefore based on a sensitivity study
120 using surface winds from recent model re-analyses and satellite analyses over the period 1996-
2018 for which satellite winds provide a reliable spatially-resolved wind dataset (both in speed and
122 direction). This temporal period also corresponds to a relatively neutral phase of the most important
climate signals in the Pacific Ocean. In particular, we intend to highlight the essential role that
124 satellite measurements can now play and in the future as a reliable source of baseline data, to help
understand the evolution and variations within these upwelling systems, a concept that has
126 proposed by previous studies but is yet to be demonstrated (Land et al., 2015, 2019; Shutler et al.,
2019).

128 Section 2 provides a description of the data sets used, a comparative analysis of the different wind
data sets, and most importantly a discussion of the data issues. Section 3 details the methodology
130 used to characterize the intensity and phenology of upwelling along the California coast, as well as
the methods applied to extract trends from time series. Section 4 aims to provide a quantitative
132 assessment of trends for some of the key biogeochemical system parameters (i.e. chlorophyll-a,
Chl-a, partial pressure of CO_2 (pCO_2) and basity or pH) and an assessment of the annual and
134 seasonal upwelling winds, with emphasis on their spatial structuring. In section 5, we highlight the
changes in the phenology of upwelling winds associated with the main Pacific Ocean climate
136 signals, in order to better analyze the interannual to near-decadal variability into which a long-term
trend of seasonal upwelling winds is shown to be embedded. A discussion follows in section 6 to
138 analyze the main results and a summary is given.

2. Data

2.1 Wind data sets

To assess the validity, strengths and weaknesses of our analysis, we have conducted a sensitivity study of our results obtained with different data sources, each with specific characteristics and limitations. Indeed, spurious climate signals can be introduced by the interaction between any biases in the atmospheric numerical model and the evolving observing system, which is a major concern in climate reanalysis (Hersbach and al., 2018). It is also challenging for multi-satellite gridded products to achieve the accuracy required for climate studies (Bourassa et al., 2019). We therefore used four popular wind datasets: two satellite surface wind analyses, the Cross-Calibrated Multi-Platform (hereafter CCMP, Atlas et al., 2011; Mears et al., 2019) version 2.0 and the Copernicus Marine Environmental Services (hereafter CMEMS, Bentamy and Croize-Fillon, 2012; Desbiolles et al., 2017), and two atmospheric re-analyses, ERAInterim (hereafter ERAI, Dee et al., 2011) and its follow-on ERA5 (Hersbach et al., 2020). The choice to add ERAI, although considered of lower quality than ERA5, is made because most recently published studies have used ERAI and because it is also used as background or first guess to help find a consistent wind field in satellite data gaps in both the CCMP and CMEMS analyses. The European Center for Medium Range Weather Forecast (ECMWF) produced native reduced-Gaussian grids for ERA5 at 31 km resolution and for ERA Interim at 80 km resolution, which have been remapped by ECMWF at 0.25° and 0.5° grid resolution, respectively, for distribution by the Copernicus Climate Change Service. The four datasets are averaged at daily resolution using the available fields every 6 hours. Both CCMP and CMEMS have a resolution of 0.25° in latitude and longitude, and use different sets of radiometer and scatterometer sensors with cross-calibration and editing of data performed independently by each data provider. The CCMP and CMEMS products are derived from very

different mapping analysis, a geostatistical analysis is used for the CMEMS products and a variational analysis for the CCMP products, but both use the ERAI winds as background. It is worth noting that, unlike the CCMP analysis, the CMEMS products do not assimilate buoys wind data and do not calculate winds over land areas. This allows independent assessment in studies using buoy as reference (e.g. Kent et al., 2013; Carvalho et al., 2014; Desbiolles et al., 2017; Wang et al., 2019; Taboada et al., 2019), avoids artifacts in the calculation of wind stress curl at locations close to buoys (Mears et al., 2019), and gives a weaker dependency on ERAI numerical winds. Indeed, near the coast, a 25-50 km blind zone exists for satellite winds that makes the CCMP coastal winds more influenced by ERAI land winds since CCMP also calculates winds over land. As any temporal trend analysis is very sensitive to the start and end points of the temporal record, the period analyzed in this study is limited to the period 1996-2018 in order to optimize the coverage of the region by scatterometers (ERS-1 and ERS-2 scatterometers in service at the beginning of 1996) and because the start and end of the period correspond to relatively calm periods for basin-scale climate variability. As only scatterometers provide near global coverage of wind direction, our choice of the period is therefore intended to limit the potential impact of the large ERAI wind biases (Belmonte and Stoffelen, 2019), within the CMEMS and CCMP products. The winds used are equivalent neutral winds at ten-meter height, and the wind stress is derived for the four wind datasets using the neutral drag coefficient proposed in Hersbach (2011).

2.2 Comparison of wind data sets and data issues

Figure 1 presents a comparison using Taylor diagram analysis of the daily alongshore upwelling winds, τ_{upw}, for the four data sources and twelve monitoring stations shown in Figure 2 and described in Appendix, Table A1. To facilitate the visualization of the Taylor diagram, the CCMP

winds are the reference to which each of the other three is compared, as they have an overall medium level of variance among the four data sets. For each station, represented by the diamond symbols in Figure 1, the data are normalized using the corresponding CCMP standard deviation, so that a normalized standard deviation less (greater) than 1 indicates a lower (greater) level of variance in upwelling winds relative to the CCMP. The results can be summarized as follows: 1) there is a small dispersion (root mean square difference, RMSD) between CCMP and CMEMS satellite winds, and a larger dispersion between satellite and model reanalysis winds; 2) CMEMS winds have slightly lower mean winds and variance; 3) significantly lower mean winds and variance are observed for the ERAI at several stations; 4) significantly higher mean winds and variance are observed for the ERA5 at almost all stations; 5) comparison statistics improve for the second half of the period, except for the ERAI, which may be the result of greater assimilation of satellite data (in particular the Advanced SCATerometers, ASCAT) in the various processes of estimating wind climatology. Note as an important feature for the following analyses, the positive wind biases of the ERA5 are strongly reduced for the second half of the temporal period.

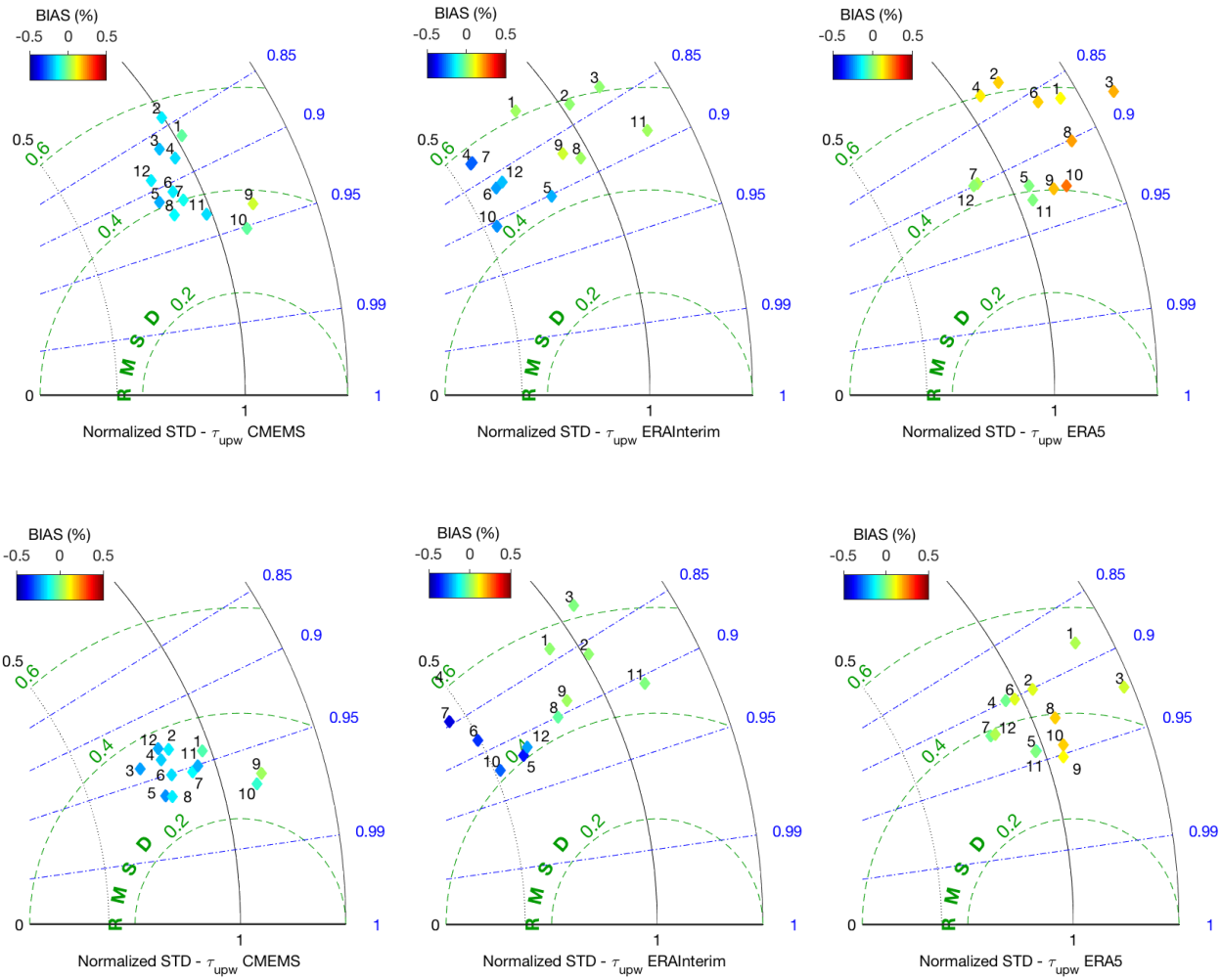

Figure 1. *Taylor diagrams for comparison of CMEMS (left panels), ERAInterim (center panels), ERA5 (right panels)* τ_{upw} *with the CCMP data. The radial axis represents the normalized standard deviation (STD), with the unit value referenced as the CCMP STD; the root mean square differences (RMSD) with respect to the CCMPdata are represented by green dashed arcs and numbers (Nm^{-2}); the correlation coefficients vary in the azimuthal direction as blue dashed-dotted lines and numbers; and the diamonds are color-coded according to the mean bias with respect to the CCMP (Nm^{-2}). Top: 1996-2006; Bottom 2007-2018.*

Complementary results are provided by an Empirical Orthogonal Function (EOF) analysis (Appendix A, Figures A1 and A2), in order to better describe the biases shown in Figure 1 between CCMP and ERA5 and their dependence on time. This analysis is applied on the monthly meridional wind stress component over the ocean-only study area. The mean seasonal cycle has not been removed because there are strong latitude-dependent time shifts in the seasonality of winds. Consequently, the EOF decomposition divides the field variance into three most significant functions representing more than 92% of the total variance, each representing a part of the study area with different time scales and phases. Overall, Figure A1 shows that the spatial patterns fit well for the CCMP and ERA5. The first EOF, EOF-1, with more than 65% of the total variance, is the leading EOF north of 38°N and explains the strong seasonality of offshore meridional winds. At station 9, near 40°N, where EOF-1 accounts for about 95% of the wind variance, (Figure A2, top panel), shows that the mean difference between the ERA5 and CCMP meridional wind stress series, reconstructed from EOF-1, is almost constant with time. The third EOF, EOF-3, accounts for only about 4% of the total variance due to low seasonality, but is the leading EOF for the coastal ocean offshore Baja California and accounts for 49.5% and 56% of the total variance at station 4 near 30°N for the CCMP and ERA5, respectively. At station 4, there is little change over time in the difference between ERA5 and the CCMP when EOF-1 and EOF-2 are used to reconstruct the meridional wind stress series (Figure A2, center panel), but a large change is observed when EOF-3 is added (Figure A2, bottom panel), that accounts for 56% and 49.5% of the variance at this station for ERA5 and CCMP, respectively. The ERA5 winds show increased temporal variance but also a stronger pattern showing opposite phase between the coastal ocean offshore Baja California and the Gulf of California. These regional differences between ERA5 and CCMP explain the mean

234 biases shown in Figure 1 and their evolution over time, and this raises the immediate question of temporal homogeneity of the data for the different data sources.

236 Indeed, although each of the wind products used in our study was developed with the objective of ensuring temporal consistency, it is poorly documented and this consistency is therefore possibly 238 unverified regionally. For satellite data, the development of climate data records for each instrument is indeed a recent concern. It is therefore challenging for multi-satellite gridded products 240 to achieve the long-term consistency, precision and accuracy required for climate studies (Bourassa et al., 2019). The challenge is related to the evolution of the observing systems that makes difficult 242 cross-calibration of the different instruments, but also to the fact that the two main multi-satellite products are dependent on another data source, i.e. the ERAI winds. To illustrate the problem, it 244 is stated on the data producer web page that the CCMP winds should not be used for studying global trends, but are suitable for studying regional trends, due to the use of ERAI winds in the 246 variational analysis scheme (http://www.remss.com/measurements/ccmp/). In addition, Desbiolles et al. (2017), although facing the same issue as the CCMP with the use of ERAI winds in the 248 CMEMS products gridding process, conducted a global trend analysis whose results are presented as consistent with other data sources and showed better comparison statistics than the ERAI to 250 buoys and QuikScat scatterometer. They note, however, that their products cannot be considered as being independent of ERAI. In addition, known effects may induce systematic differences 252 between model reanalysis and satellite analysis products. Indeed, environmental factors such as surface currents, sea state and local air-sea interactions are known to affect scatterometer 254 measurements (Quilfen et al., 2001, 2004; Chelton and Xie, 2010; Kent et al., 2013; Bourassa et al., 2019; Mears et al., 2019) and contamination of satellite measurements by rain can still be a 256 problem despite quality control and rain flagging. For the numerical model winds, the surface

winds from the 4-D model reanalysis are likely to be affected by several possible biases other than
258 those that related to the calibration and editing of assimilated ocean surface wind data. As stated in Hersbach et al. (2018), erroneous climate signals can be introduced by the interaction between
260 atmospheric numerical model bias and the evolving observing system, which remains a major concern in climate reanalysis. Any bias in the system can propagate and impact surface winds
262 through the 4D variational analysis. As the oceans are relatively poorly instrumented with buoys, a recognized primary reference for surface wind data is provided by scatterometer instruments for
264 which cross-calibration of different missions over time can be carefully performed. Belmonte and Stoffelen (2019) showed and discussed the biases of several ms^{-1} in the ERAI and ERA5 winds
266 relative to ASCAT scatterometer, with a strong latitudinal dependence. However, they also showed that the ERA5 is a significant improvement over ERAI in this regard.

268 Another caveat regarding the use of these wind data sets for the study of coastal upwelling is the systematic data contamination by parasitic land effects due to the coarse resolution and poor
270 land/sea transition profiles for the atmospheric model winds (Taboada et al., 2019; Belmonte and Stoffelen; 2019), and because the 25-50 km coastal blind zone for satellite winds makes gridded
272 satellite winds (wind stress vector and curl) more sensitive to land contaminated ERAI nearshore winds. In this regard, and because CCMP also analyzes winds over land, CCMP coastal winds may
274 be largely constrained and contaminated by over-land ERAI winds, especially during periods of scatterometer data gaps for which the blind zone of satellite data is approximately 50 km.

276

278

2.3 Chl-a and carbonate system data sets

We are using two global reference datasets to assess trends in the California upwelling biogeochemical system. The Chl-a concentration is produced at a monthly and 4-km resolution by the Ocean Colour Climate Change Initiative project (OC-CCI, Jackson et al., 2019), covering the period 1998-2018. The surface partial pressure of carbon dioxide in seawater (pCO_2) and seawater pH produced at a monthly and one-degree resolution is referenced as the Global Ocean Surface Carbon Product by the CMEMS project (Denvil-Sommer et al., 2019; Chau et al., 2020), and we used the 2020 version covering the period 1985-2018. pCO_2 was estimated using a feed-forward neural network to reconstruct monthly values from a pCO_2 climatology and input variables known to be the main physical, chemical and biological drivers: sea surface temperature and salinity, sea surface height, mixed layer depth, chlorophyll-a concentration, and the atmospheric CO_2 mole fraction. The pH was calculated from pCO_2 and the reconstructed surface ocean alkalinity whose time- and space-varying fields were obtained by a multivariate linear regression with salinity, temperature, dissolved silica and nitrate as independent variables.

3. Methods

To evaluate upwelling intensity and its dependence on latitude, upwelling winds and derived Ekman transport were calculated for a series of twelve stations located every two degrees of latitude along the coast, approximately 100 km from the coast, which corresponds roughly to the boundary between the nearshore and offshore upwelling zones. These choices also avoids systematic contamination of data by parasitic land effects due to the coarse resolution and poor land/sea transition profiles of numerical winds, and also due to the 25-50 km coastal blind zone for satellite winds that makes the gridded satellite winds (wind stress vector and curl) more sensitive to

inaccurate nearshore ERAI wind data. Furthermore, the effective resolution of gridded satellite winds is no better than 100 km (Desbiolles et al., 2017), and even coarser for model winds, to make our choice of station locations appropriate. Figure 2 shows the location of the stations, with the seafloor elevation, and the mean annual Ekman transport and curl-driven velocity calculated using the CMEMS data. Table A1 in Appendix A provides specific information on stations location. The location of each station is chosen to correspond exactly to the latitude and longitude of a specific grid point in the CMEMS and CCMP grids, and the nearest ERA5 and ERAI grid points to the station coordinates were selected to avoid unnecessary interpolation. The selection of the nearest pixel in the grid does not introduce significant differences since the effective resolution is much coarser than the co-location distance. The same approach was applied to pH and pCO_2 data in that the selected pixel in the grid is that which is the closest to the coast. For Chl-a, we averaged the 4 km resolution data over an area of 50 (100) km square offshore (around) the location of coastal point (station) to obtain the coastal and offshore values for Chl-a at each station. For coastal Chl-a, the coastal point is determined by the perpendicular distance between the coast and the intersecting the station.

Two main wind-driven processes determine the dynamics of EBUS, the coastal divergence of mass transport induced by the along-shore component of wind stress, defined as the cross-shore Ekman transport, and the vertical velocities associated with the wind stress curl, defined as the Ekman pumping/suction (e.g. Halpern, 2002; Capet et al., 2004). The first occurs at a cross-shore scale limited to a few tens of km from the coast (Estrade et al., 2008) while the second can extend over a few hundreds of km. Both processes are quantified using solutions from Ekman's model (Ekman, 1905) as follows:

1) The upwelling driven by the alongshore equatorward component of the wind stress, causing coastal divergence, is expressed by the cross-shore Ekman transport:

$$EKT = \tau_{upw}/\rho f \quad (1)$$

where τ_{upw} is the alongshore equatorward component of the wind stress. The unit of EKT is given in m^3s^{-1} per 100 m of coast length.

We also use a Cumulative Upwelling Index (CUI) that is calculated as the integration of the daily EKT along the Julian day of each year, and a Total Upwelling Magnitude Index (TUMI) calculated as the difference between the CUI values at the beginning and end of the upwelling season, as proposed in Bograd et al. (2009). To determine the beginning and end of the upwelling season, a 40-day Lanczos low-pass filter was first applied to the daily CUI records, and inflection points are searched for in prescribed time windows. This index accounts for the strong changes in the seasonality of the upwelling.

2) The upwelling caused by the wind stress curl is expressed by the vertical velocity at the base of the Ekman layer:

$$W = (curl\tau)/(\rho f) + (\beta\tau_x)/(\rho f^2) \quad (2)$$

where curlτ is the wind stress curl, $\rho = 1.025\ kg.m^{-3}$ is the air density, $f = 2\Omega\sin\phi$ is the Coriolis parameter, Ω is the angular speed of the earth, and ϕ is the latitude. The second term on the right side of the equation is a correction term for the β plane effect (derivative of f with latitude), and τ_x is the zonal component of wind stress. The unit is usually given in m s^{-1}, cm day^{-1}, or m day^{-1}. A positive upward (negative downward) value of W is called Ekman suction (pumping).

348 The water transport associated with the wind stress curl can be estimated as the integration of W
from coast to a given offshore location where the wind stress curl vanishes. In the CCUS, wind
350 stress curl driven transport can be of the same order of magnitude as the Ekman transport EKT
(e.g. Halpern, 2002; Pickett and Paduan, 2003). Wind stress curl is an ubiquitous feature in the
352 CCUS due to the drop in wind stress at the coast, generated by the frictional retardation by land,
and to wind disturbances usually observed in the lee of major headlands along the California coast
354 (e.g., Cape Blanco, Cape Mendocino, Pt Arena, and Pt Conception), as shown in Figure 2, center
panel.

356 Since there are no accurate long-term measurements of coastal winds over the entire CCUS to
properly quantify these two upwelling processes, and given the relatively coarse effective spatial
358 resolution of our wind data sets (no better than 100 km), we therefore monitor upwelling at the
selected locations using EKT and W indices as first-order approximations or descriptions of the
360 upwelling intensity, as was done in previous studies based solely on wind or surface pressure data.
This implies some simplifications related to relevant upwelling dynamics as discussed in Estrade
362 et al. (2008) and Marchesiello and Estrade (2010) which have shown that the upwelling intensity
can be significantly limited by onshore geostrophic flow. Based on these results, Jacox et al. (2018)
364 defined a new upwelling index for the California Current System, the Coastal Upwelling Transport
Index (CUTI), which formally accounts for the geostrophic flow competing with the offshore
366 Ekman transport. The geostrophic and Ekman transports are computed using the outputs of the
high resolution Regional Ocean Modeling System (ROMS) with a surface wind forcing that
368 combines CCMP for the earliest period 1988-1998 and outputs from the high-resolution Coupled
Ocean/Atmosphere Mesoscale Prediction System for the most recent period. This does not result
370 in a single self-consistent reanalysis for our period 1996-2018 and we therefore did not include this

recent upwelling indicator for our trend study, mostly because CCMP coastal winds are likely
372 erroneous as discussed in section 2.2. However, Ding et al. (2021) showed that, in the context of global warming on long time scales, future changes in cross-shore geostrophic transport associated
374 with changes in sea surface height along the California coast should certainly be better accounted for in upwelling trends analyses. Our approach using a first-order proxy for upwelling intensity at
376 100 km distance from the coast, where satellite data are not contaminated by land, can be further justified. Indeed, Jacox et al. (2014) showed that the mean upwelling transport and its trend,
378 depicted using EKT indices based on CCMP winds, closely follow results obtained with the vertical transport over a 200 km wide coastal strip, calculated using ROMS vertical velocities. They
380 showed, however, that this EKT proxy is biased high on average by ~ 25% in the central CCUS, an amount corresponding to the onshore geostrophic transport, and also showed that this is a more
382 realistic estimate of upwelling intensity than the classical Bakun index (Bakun, 1973) based on the surface pressure fields of a low-resolution numerical model. Furthermore, it has also been shown
384 for a recent period that long-term changes in upwelling intensity are related to changes in large-scale winds since there is a high temporal coherence along the coast between the Ekman
386 pumping/suction and coastal divergence (Renault et al., 2015). For our analysis period, indices based on large-scale winds are therefore thought to be relevant for predicting the overall tendencies
388 in coastal marine productivity (Renault et al., 2016; Turi et al., 2016).

390

392

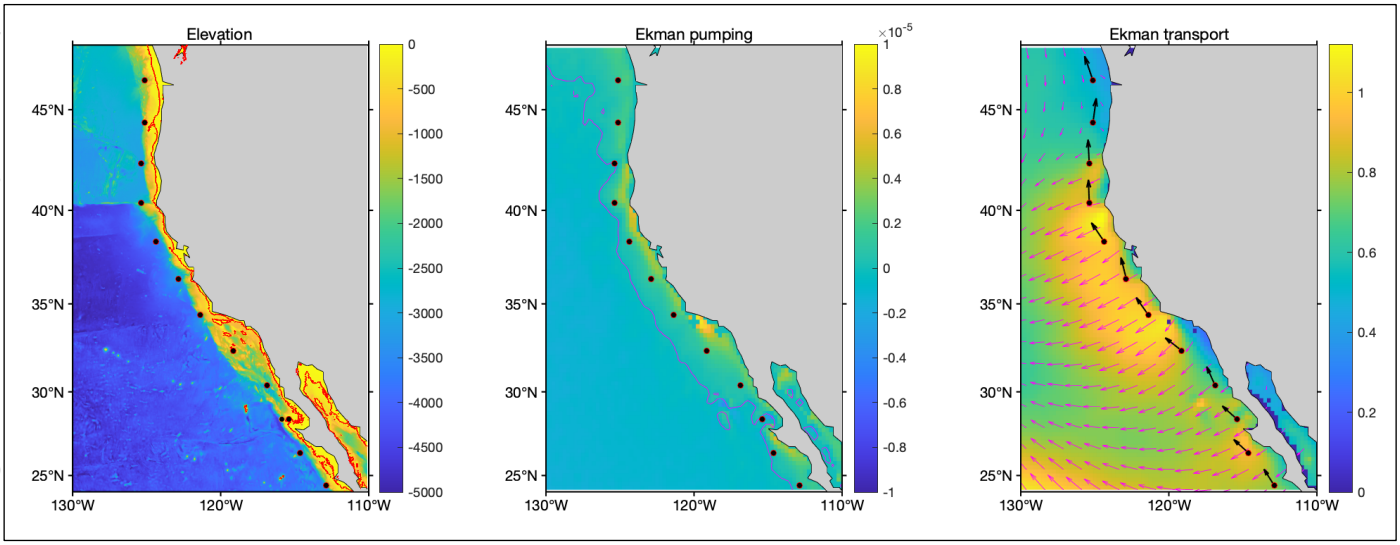

Figure 2. *Location of the twelve stations (dots) and seafloor elevation (left, m), mean Ekman vertical velocity (center, ms^{-1}, zero-contour as a magenta solid line), and mean Ekman transport (right, m^2s^{-1}, black arrows indicate the orientation of the coastline used to derive* τ_{upw}*)*

In this paper, temporal trends are analyzed primarily using the most widely used non-parametric Seasonal Mann-Kendall Trend Test (hereafter SKTT, Hirsch et al., 1982; Hirsch and Slack, 1984), and the associated Sen's slope estimate (Sen, 1968; Young and Ribal, 2019), which is a randomness versus trend test that has been shown to be robust in comparison to parametric alternatives for realistic stochastic processes (exhibiting seasonality, skewness and serial correlation). Since perfectly linear trends rarely describe realistic evolution patterns of complex meteorological processes, reducing the indication of possible monotonic trends given by SKTT to that of a linear trend by the Sen's slope is certainly too restrictive and should be kept in mind. The statistical significance of the estimated trends is tested and shown at $p < 0.1$ in section 4 for a graphical representation, and the p-values are given in section 5 when non-parametric and parametric approaches are used. However, the interpretation of trend tests and associated p-values should

always be taken with caution and the following statement by Serinaldi et al. (2018), who discussed the issues related to trend tests at length, served as guideline in this study: "If a clear physical mechanism related to a predictable evolution of the properties of the process at hand is not identified, we cannot make conclusions about the reason of rejection or lack of rejection, since multiple factors not included in the null and alternative hypotheses can actually play a role".

4 Overall trends in the California Current Upwelling System

4.1 Basin-scale climate variability

The trends observed and discussed in the following sections should be placed in the context of natural basin-scale climate variability that imposes a remote forcing of the CCUS at interannual and near-decadal scales. Indeed, while studies predicting long-term changes in upwelling intensity (Bakun, 1990; Bakun et al., 2015; Rykaczewski et al., 2015) have generated considerable interest in studying upwelling trends in the CCUS using historical data, as in Sydeman et al. (2014) for the period 1990-2012, such a period is certainly too short to obtain robust results on long-term changes associated with human activity, or it may simply be out of context if the forced changes emerge later in the 21st century (Brady et al., 2017). Three main interconnected climate signals exert remote control over the CCUS variability: the North Pacific Gyre Oscillation (NPGO), the Pacific Decadal Oscillation (PDO), and the El Niño-Southern Oscillation (ENSO), and this topic has been widely discussed in many studies (e.g. Di Lorenzo et al., 2008; Bograd et al., 2009; García-Reyes and Largier, 2012; Chenillat et al., 2012; Meinvielle and Johnson, 2013, Jacox et al., 2015; Kahru et al., 2018; Bonino et al., 2019). Figure 3 shows that, for our analysis period 1996-2018, the PDO and ENSO are in a near neutral phase at the beginning and end of the period, while the NPGO is

negative at both times. Overall, the NPGO and PDO show quasi-decadal variability, visibly anti-correlated, with abrupt phase changes for both indices (e.g. 1997/1998, 2004/2005, 2014/2015). The NPGO (PDO) is in average positive (negative) for the periods 1999/2003 and 2008/2013. The ENSO shows interannual variability with strong warm El-Niño events in 1997/1998 and 2015/2016, and weaker warm events in 2002 and 2010.

At the beginning and end of our period, 1996-2018, there is no particular signature of these basin-scale climate signals that is likely to influence our trend analysis.

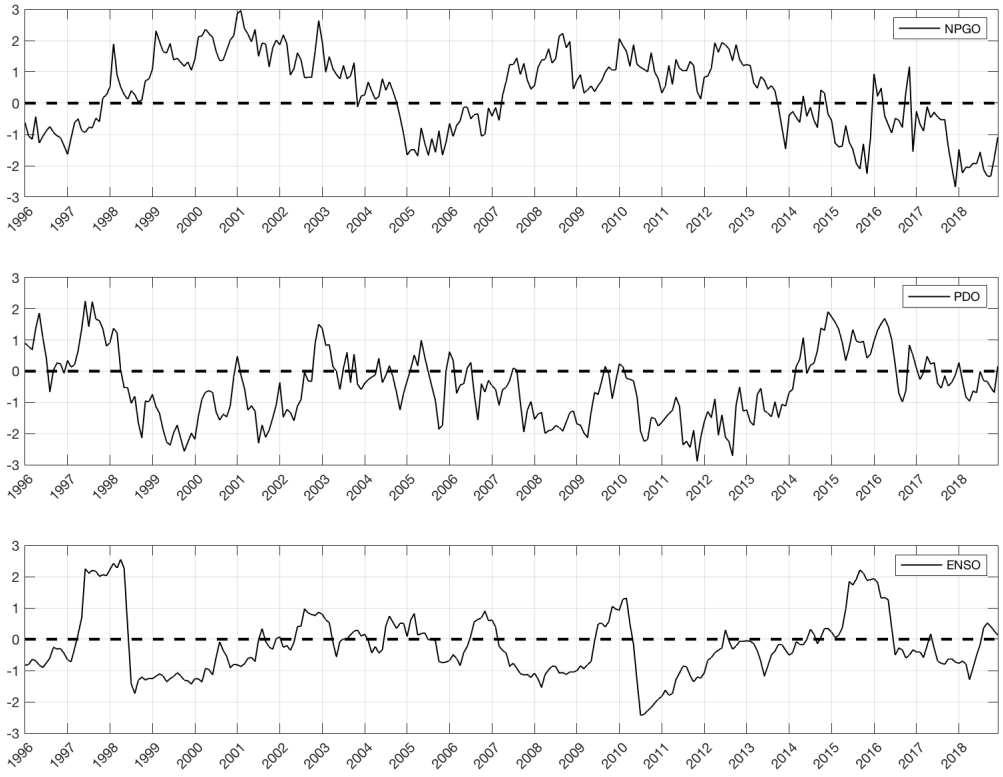

Figure 3. *Monthly values of climate indices: top, North Pacific Gyre Oscillation (NPGO) index, center, Pacific Decadal Oscillation (PDO) index, bottom, multivariate El Niño Southern Oscillation (ENSO) index.*

4.2 Observed trends in Chl-a, pCO_2, and pH

Changes in the CCUS marine eco-system are subject to continuous monitoring and many studies involving in-situ measurements (e.g. Iles et al., 2012; Chan et al., 2017; Chavez et al., 2017) and numerical modelling of the coupled physical-biogeochemical ecosystem (e.g. Gruber et al., 2012; Hauri et al., 2013; Lachkar, 2014; Turi et al., 2016). But few global observational datasets are available to characterize its long-term evolution. Past efforts and recent developments have led to the provision of climatologies for some of the main biogeochemical parameters.

Figure 4 shows trends in Chl-a, pCO_2 and pH estimated from the high-resolution OC-CCI dataset for Chl-a and the lower-resolution CMEMS dataset for pCO_2 and pH, all of which are key variables in the marine ecosystem. Chl-a is used as a central metric of phytoplankton biomass and as a proxy for Net Primary Productivity (NPP), and pH is a key parameter for monitoring changes in the marine carbonate system with respect to ocean acidification. Annual mean Chl-a concentrations vary most strongly in the cross-shore direction, with a littoral ribbon of elevated Chl-a showing a seasonal cycle in opposite phase (Deutsch et al., 2020). Figure 4, left panel, thus shows the trends observed for the offshore and nearshore (< 50 km) areas of the CCUS. The trends (with $p < 0.1$ intervals indicated) are observed nearshore with high latitudinal variability, showing an increase (decrease) in Chl-a concentration north (south) of 32°N during the period 1998-2018. The observed trends in Chl-a and pH for the northern CCUS are comparable to those obtained in Turi et al. (2016) for the period 1997-2011, although their analysis did not cover the CCUS south of 30°N and therefore did not analyze the negative trends shown nearshore south of 30°N in Figure 4. The central and bottom panels in Figure 4 show trends in pCO_2 and pH, respectively, for the data pixel closest to the coast. At one-degree resolution, the CMEMS dataset does not clearly separate the nearshore area, whereas stronger trends are expected in the 100 km nearshore area (Turi et al.,

476 2016). Trends are presented both for the full period covered by the dataset, 1985-2018, and for the 1998-2018 period covered by the Chl-a dataset. The positive (negative) trends in pCO_2 (pH) 478 suggests that the carbonate system in the CCUS is subject to strong latitudinal variability, as for Chl-a, and to faster change for pH during the period 1998-2018. For this period, the largest decrease 480 in pH, > 0.002 yr^{-1}, is observed between 35°N and 42°N (42° is the boundary latitude where downwelling conditions prevail on average). Turi et al. (2016) obtained comparable results from 482 numerical modelling experiments, although they vary significantly with the forcing wind product, and suggested that the decrease in nearshore pH, and its latitudinal regionality, is mainly due to 484 local increase in Dissolved Inorganic Carbon (DIC). Combined with the primary effect of increasing atmospheric CO2 uptake, upwelling intensification is proving to be a robust driver for 486 further increase in acidification and aragonite undersaturation in the CCUS (Lachkar, 2014; Chan et al., 2017), which is consistent with the pCO_2 and pH trend patterns in Figure 4. Changes in 488 biological productivity are also strongly related to changes in intensity and timing of upwelling, but other geochemical and environmental factors are of primary importance, particularly nitrate 490 concentration, and robust dome-shaped relationships between the different drivers have been identified (e.g. García-Reyes et al., 2014; Jacox et al., 2016). Therefore, the Chl-a trends presented 492 in Figure 4 cannot simply be related to trends in upwelling winds.

494

496

498

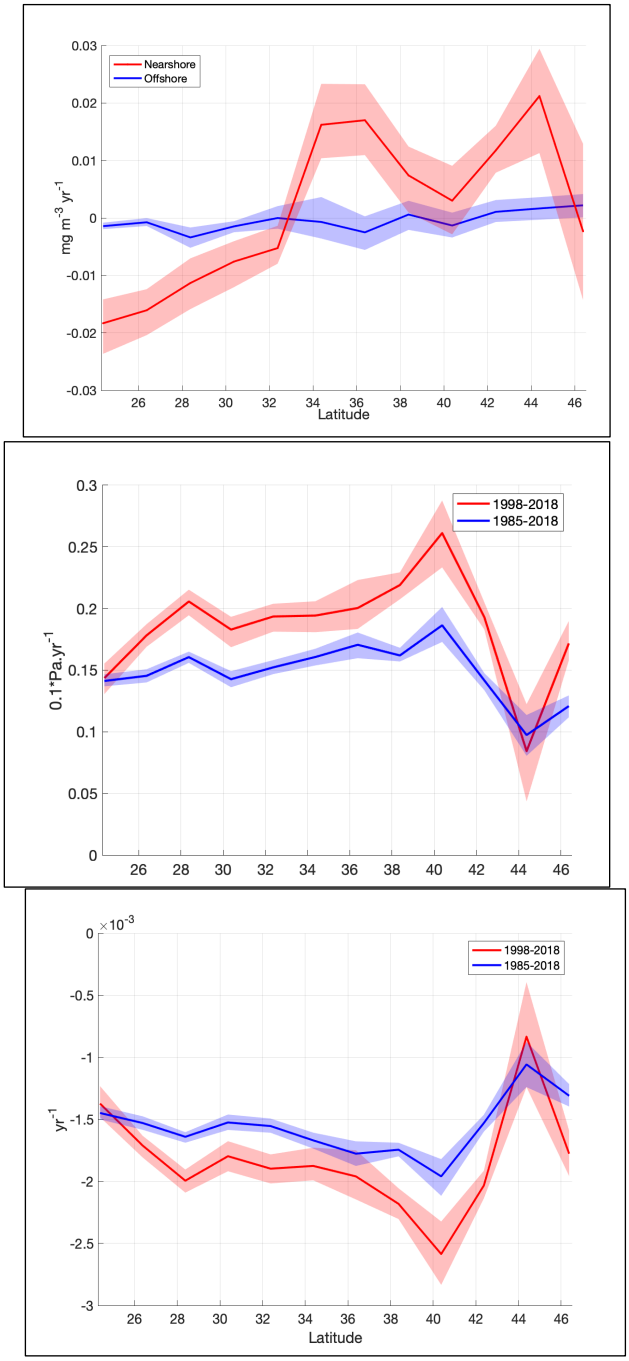

Figure 4. *top panel: trends in Chl-a (mg m^{-3} yr^{-1}) nearshore (distance to coast < 50 km, red solid line) and offshore (75 km < distance to coast < 150 km, blue solid line) for the period 1998-2018. Central and bottom panels: trends in pCO_2 (central panel, 0.1Pa yr^{-1}) and pH (bottom panel) for the periods 1998-2018 (red solid line) and 1985-2018 (blue solid line). The colored areas correspond to a p-value < 0.1.*

522 To place the estimated trends in the context of the Pacific Ocean basin, examples of the high variability observed in the seasonal cycle of Chl-a are shown in Figure 5. Different reference
524 seasons are defined as in García-Reyes and Largier (2012): the winter season (December-February), the upwelling season (April-June), and the relaxation season (July-September). The
526 months of March, October and November are considered as transition periods. For Chl-a, there is overall little shift in seasonality in the northern and southern CCUS, with Chl-a values peaking
528 during the upwelling or relaxation seasons depending on latitude, with some notable exceptions such as the much longer upwelling season in 2002 and 2003 near 29°N associated with much higher
530 than usual Chl-a values, or in 2005 near 40°N. Conversely, there is a high variability in the central CCUS and Southern California Bight, where the peak of Chl-a occurs in almost all seasons. There
532 is generally greater variability in maximum values than in minimum values at all locations and several noteworthy events can be related (Di Lorenzo et al., 2008) to the relative influence of the
534 PDO, strong north of 38°N, the NPGO, strong south of 38°N, and ENSO. Thus, at 40°N, Chl-a is above average during the upwelling/transition seasons from 2001 to 2005 and below average from
536 1998 to 2001 and from 2006 to 2013, the latter periods corresponding to a positive phase of the PDO. Between 37°N and 33°N, the large positive anomalies in 2005 and 2006 can be related to the
538 remote forcing associated with a negative NPGO, although this was not observed in 2018 when NGPO was also strongly negative. Finally, the strong El Niño events of 1997/1998 and 2015/2016
540 and the marine heat wave, known as the "Blob event", of 2014-2015 obviously strongly impact the Chla south of 35°N.

542 Kahru et al. (2018) correlated the variability of Chl-a during these warm events with the frequency of SST, Chl-a fronts and the spring onset of upwelling. Jacox et al. (2016) also analyzed several
544 anomalous wind-driven events during the period 1998-2010 to describe the optimal environmental

conditions prevailing for biological productivity, and to define a framework for the bottom-up control of the productivity by the wind stress and nitrate concentration drivers. They showed that basin-scale remote forcing and changes in the upwelling season timing are of primary importance. In the following sections, we therefore focus on trends in upwelling winds and changes in upwelling phenology that may result from basin-scale remote forcing or long-term wind changes, and that impact the CCUS biogeochemical ecosystem.

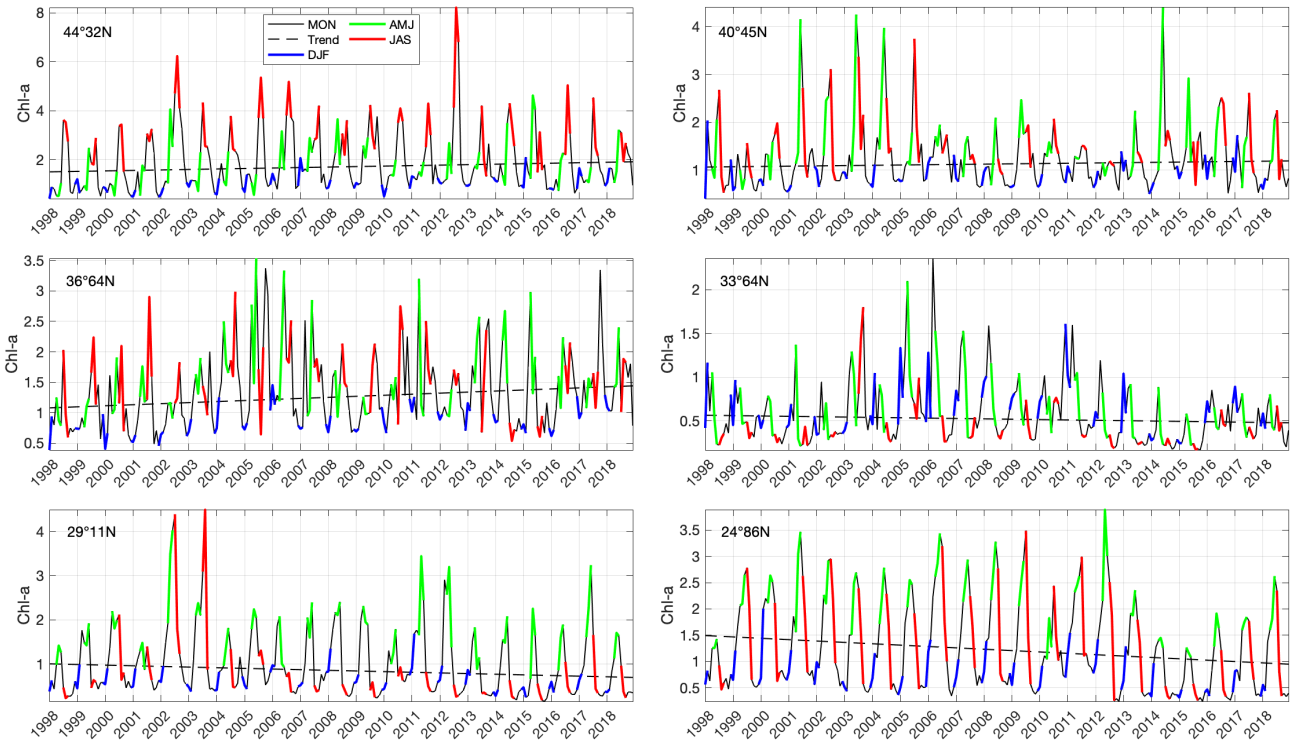

Figure 5. *Monthly values of coastal Chl-a (mg m^{-3}, averaged over a distance to coast < 50 km) for the periods 1998-2018, and seasonal values such as: December/January/February (DJF, blue line), April/May/June (AMJ, green line), July/August/September (JAS, red line). March/October/November (MON, black line). The dashed black lines show the trend as estimated in Figure 4. The latitude shown in the upper left corner of each plot is the latitude of the coastal*

point located on the perpendicular to stations 1, 3, 5, 7, 9, 11 from bottom-right to top-left (see Table A1 for details).

4.3 Observed trends in upwelling winds

Although the main driver of ocean acidification is the accumulation of anthropogenic CO_2 from the atmosphere, climate fluctuations can enhance or mitigate this acidification trend within the EBUS, and the assessment of this trend is therefore highly dependent on the choice of start and end years for the time record being analyzed. For example, a strong El Niño signal prevailed during the winter of 1997-1998 (see Figure 3), which is associated with stronger southerly winds during winter in the northern CCUS, a delayed upwelling season, and a reduction in equatorward upwelling-favorable winds in central and northern CCUS (Jacox, 2014; Turi et al., 2016). Other human-induced changes are predicted, including an increased contrast between atmospheric pressure over the ocean and land, leading to an increase in upwelling winds (Bakun, 1990), or, more recently, a long-term poleward shift of ocean high pressure systems, leading to a long-term increase (decrease) in summer upwelling-favorable winds in the northern (southern) CCUS (Bakun et al., 2015; Rykaczewski et al., 2015), both of which are likely to contribute to changes in the carbon system.

The objective of this work is thus to link this observed large-scale trend in biogeochemical parameters, and its latitudinal structuring, to atmospheric forcing. To do so, and as indicated in the data section, the approach chosen is based on the use of different state-of-the-art wind data sources and on an appropriate choice of the beginning and end of the analyzed period in order to ensure a good coverage by satellite winds while minimizing effects of the main climate signals.

Average alongshore winds are favorable for upwelling, except north of 44°N where downwelling conditions prevail slightly on average at our two northernmost stations, as shown on the average Ekman transport chart (Figure 2, right panel). For greater clarity, the trends estimated using the SKTT over the period 1996-2018 and the associated $p < 0.1$ confidence limits are presented separately in Figure 6 for the numerical models winds (left panels) and for the analyzed satellite winds (right panels). The upper panels show the estimated annual trends at each station, using the SKTT and monthly time series over all seasons. This is computed as the median value of the trend obtained using Sen's regression applied to each of the twelve months concurrently to estimate a single trend. Thus, this SKTT configuration is specifically designed to provide a single summary statistic for the entire record and will not indicate when there are differing trends in different months or seasons. To study trend seasonal dependence, the bottom panels therefore show independently estimated seasonal trends for the three characteristic seasons defined in section 4.2. Overall, from the upper panels, a very similar behavior is obtained for CCMP and CMEMS satellite winds, showing stronger upwelling-favorable winds between 34°N and 42°N, an area located approximately between Point Conception and Cape Blanco. The model winds also show a similar trend at these locations, but with lower levels of significance, and show a trend towards reduced upwelling winds in the southern part of the CCUS that is not observable in the satellite data.

The seasonal analysis shows, in lower panels of Figure 6, a better agreement between the model reanalysis products and the satellite analysis products for the winter season for which upwelling-favorable trends of comparable magnitudes are found between 35°N and 45°N. South of 33°N, weaker trends of reduced upwelling winds are found with $p < 0.1$ for ERA5, ERAI, and CMEMS at different locations. For the upwelling season, comparable upwelling-favorable trends are also found between about 38°N and 43°N with satellite and model reanalysis products, but with

602 different levels of significance. South of 33°N, trends towards reduced upwelling winds ($p < 0.1$) are found with ERA5. For the transition season, no trend at $p < 0.1$ is observed with the satellite
604 products, while trends towards reduced upwelling winds with $p < 0.1$ are observed with ERA5 and ERAI at several locations in the southern zone. In summary, trends of stronger upwelling winds
606 are consistently found during the winter and upwelling seasons, between about 35°N and 45°N, and equivocal results are found in the southern zone, with trends of reduced upwelling winds being
608 only identified within the model reanalysis products. This difference in trends is reflected in the evolution over time of the comparison statistics between the models and the satellite winds (Figure
610 1). Indeed, for the ERA5 alongshore winds at southern stations (1 to 4), the high bias with the CCMP was significantly reduced between the first and second half of the analysis period. For the
612 ERAI and stations 4 to 7 between 30°N and 36°N, the low bias with the CCMP increased. However, these observed differences are consistent with results presented in Belmonte and Stoffelen (2019)
614 in which the weaknesses of the ERA5 and ERAI are discussed at global and local scales. They further show that the ERA5 is however a significant improvement over the ERAI.

616

618

620

622

624

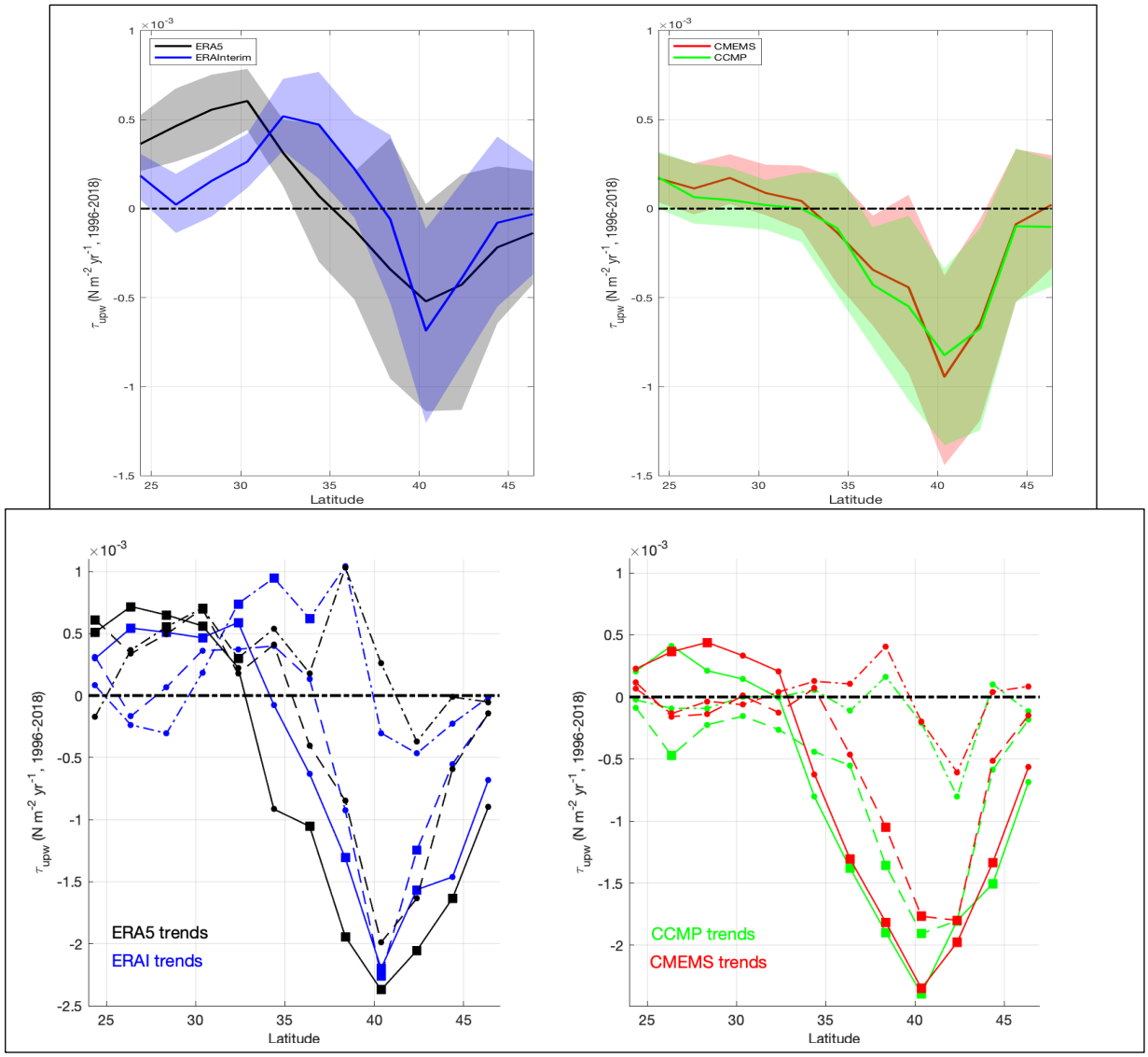

Figure 6. *Top panels: Annual τ_{upw} trends (N.m^{-2} per year, negative for increasing equatorward winds) as a function of latitude, for the twelve stations, over the period 1996-2018, for model winds (left panel) and satellite winds (right panel).The color-shaded areas correspond to p-value < 0.1. Bottom panels: Seasonal τ_{upw} trends (N.m^{-2} per year) over the same period and on the same x-axis for model winds (left panel) and satellite winds (right panel), for the winter season (solid lines), the upwelling season (dashed lines), and the transition season (dashed-dotted lines). Filled squares indicate p < 0.1. The color code follows ERA5 in black, ERAI in blue, CMEMS in red, CCMP in green.*

Alongshore wind stress is the main driver for coastal upwelling, but the wind stress curl caused by the wind slackening at coast or by reduced intensity downwind of headlands (i.e. a wind shadowing) is another important source of vertical velocities. In Figure 7, the mean annual curl-driven transport, integrated from the coast to each station, is presented for only three of the data sources because the ERAI resolution does not allow for such integration. This shows that upwelling conditions prevail on average south of 44°N, with significant differences between the satellite-derived and ERA5 transports. These can be related to the systematic differences in wind stress curl already shown in Belmonte and Stoffelen (2019). The curl-driven velocities and associated transport show the same trend structuring as for the alongshore winds in Figure 6, with a comparable level of uncertainty, which is the result, on average, of the strong correlation between the increase (decrease) of offshore winds and the increase (decrease) of the wind stress curl. So overall, the results of trend analysis using satellite and model analyses are contradictory in the southern part of the CCUS.

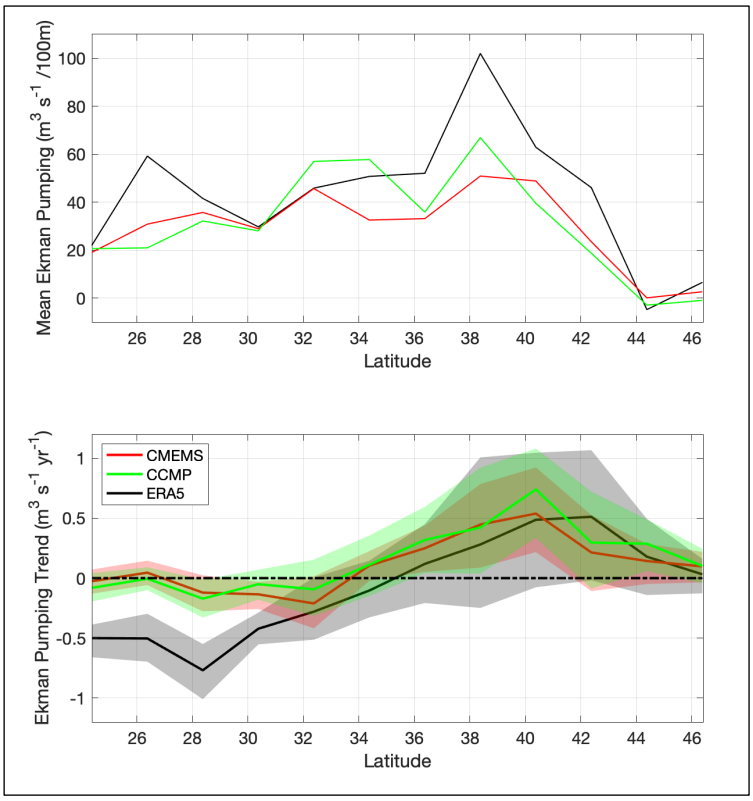

Figure 7. *Top panel: average integrated Ekman pumping transport (m^3s^{-1} per 100m of coast) as a function of latitude, for the twelve stations, averaged over the 1996-2018 period. Lower panel: associated trends (m^3s^{-1} per year) over the same period and same x-axis for ERA5 in black, CMEMS in red, CCMP in green.*

The spatial structuring of the trends observed in our study can be related to the trends obtained for the biogeochemical parameters in Figure 4. Increased upwelling favorable winds are associated with increased Chl-a concentrations, decreased pH and increased pCO_2 between 36°N and 42°N. South of 34°N, results obtained with the different wind datasets diverge.

In the next section, we analyze in-depth changes in the CCUS phenology associated with large-scale climate fluctuations, in order to better identify the possible long-term trends in CCUS intensity associated with the trend in upwelling winds that have been consistently found in this section.

5. Changes in the upwelling phenology

The marine ecosystem of the EBUS is largely influenced by the seasonality of upwelling winds and more specifically by the phase and intensity of upwelling favorable winds, i.e. the phenology of upwelling. Indeed, large scale climate signals modulate the seasonality of the CCUS and the key climate signals discussed in section 4.1 are correlated with changes in the phenology of the CCUS (e.g. Di Lorenzo et al., 2008; Bograd et al., 2009; García-Reyes and Largier, 2012; Chenillat et al., 2012; Meinvielle and Johnson, 2013, Bonino et al., 2019).

Bograd et al. (2009) analyzed these influences by mapping of a cumulative upwelling indice, CUI, and other within-season indices. The CUI is computed as the integration of the daily cross-shore

Ekman transport along the Julian day of each year. Since upwelling winds have a cumulative effect on ecosystem productivity through the provision of nutrient-rich waters, the CUI itself can provide useful information on changes in ecosystem productivity, although it is only one of the primary factors relating to net primary production and linked to nutrient supply (García-Reyes at al., 2014; Jacox et al., 2016). Here we seek to analyze long-term changes in the seasonality of upwelling for two of the stations where the wind trends were consistently found at $p < 0.1$ (Figure 6). Figure 8 shows the upwelling winds and associated CUI at 30°375 N and 40.375° N, where a trend towards less favorable upwelling winds was found with ERA5 and ERAI at the southern location, and a trend towards stronger upwelling winds was found with CCMP and CMEMS at the northern location.

The upper panels show, for 30°375 N, the large difference between the ERA5 alongshore winds and the satellite winds at the beginning of the period, as discussed in the previous sections, with the ERA5 CUI being significantly larger than other CUIs until about 2002. At 30°375N, the CUI increases continuously each year, indicating almost constant equatorward winds, with a clear decadal modulation in the maximum of the CUI. For all data sources, the CUI tends to be higher for the negative (positive) phases of the PDO (NPGO) and also higher for some of the strong La Niña conditions that followed El Niño events such as in 1998-1999 and 2010-2011.

At 40°375N, the interannual variability is strikingly illustrated by the annual mapping of CUI and the signatures of the ENSO and PDO are clear. In central and northern CCUS, El Niño years are associated with stronger southerly winds in winter, leading to minima in CUI which appear to be related to the strength of ENSO, as in 1997/1998, 2009/2010, and 2015/2016. Typically, El Niño years are followed by cold phases of the PDO during which the northerly winds are weaker in

winter, the upwelling season begins earlier and the maximum CUI increases until another positive ENSO occurs.

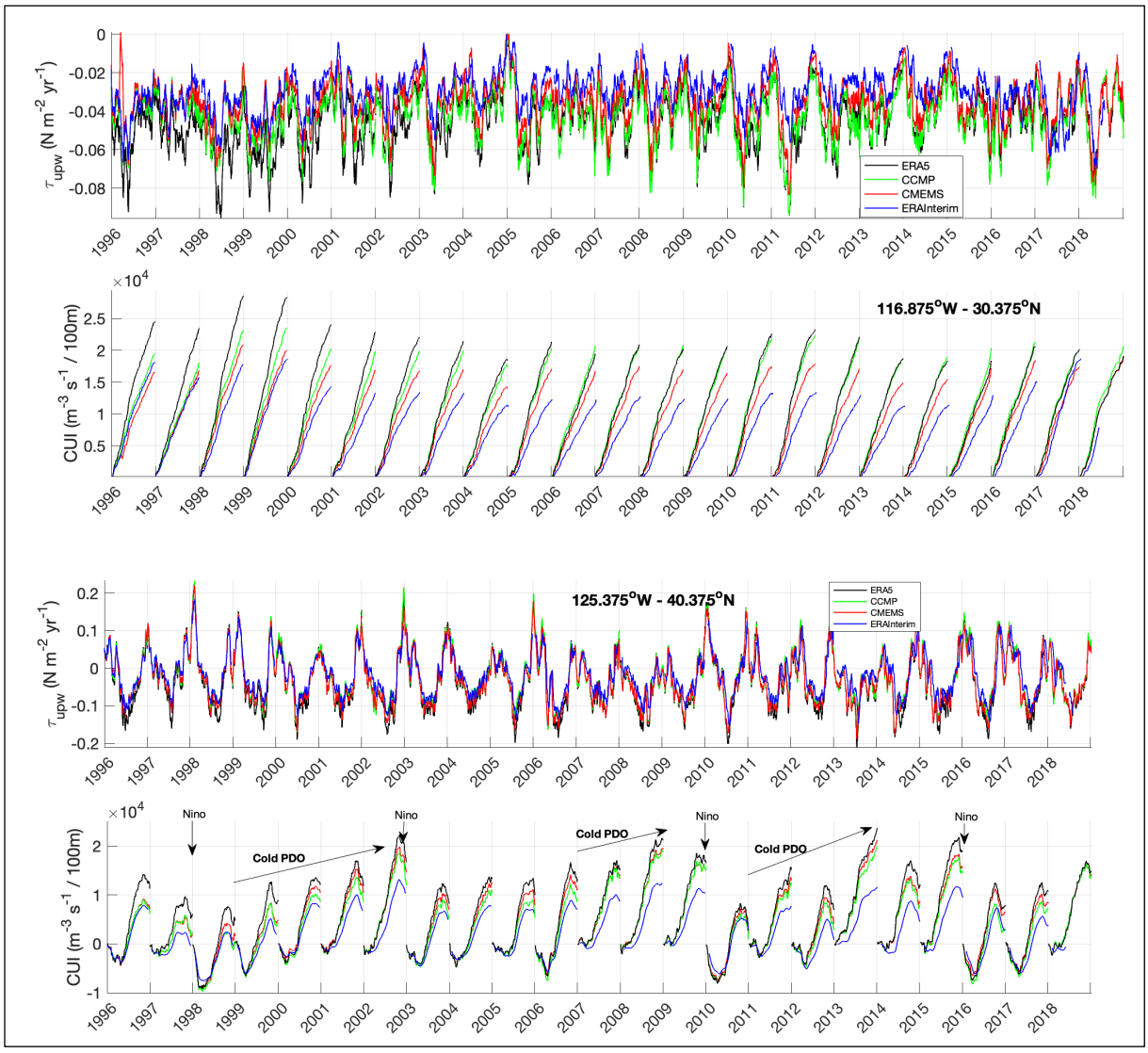

Figure 8. *Mean alongshore upwelling winds (τ_{upw}, N.m^{-2}, negative when equatorward) and associated CUI (m^{-3}.s^{-1} / 100m) as a function of time, at 116°875W – 30°375N (top panels) and 125°375W – 40°375N (bottom panels). The color code follows ERA5 in black, CMEMS in red, CCMP in green, ERAInterim in blue.*

738 These significant changes in CCUS phenology associated with large-scale climate signals make it difficult to detect long-term trends in upwelling forcing, although 1996 and 2018 can be considered
740 relatively neutral years in this regard. Therefore, to investigate this issue further, we use the Total Upwelling Magnitude Index (TUMI, see the Methods section) calculated as the difference between
742 the CUI values at the beginning and end of the actual upwelling season, as proposed by Bograd et al. (2009). This index takes into account the large variations in the upwelling seasonality and
744 therefore better represents the actual cumulative effect of upwelling on ecosystem productivity than a conventional integration of upwelling winds over a fixed upwelling season (usually April to June
746 or July). In addition, this index was also tested by integrating only over upwelling favorable daily transports during the actual upwelling season; this had no significant impact on the following
748 results. The first two panels in Figure 9 show, for the four sources of wind data, the TUMI as a function of the year at the two stations analyzed in Figure 8. The two lower panels show the
750 detected duration and start time of the upwelling season at 40.375°N only, since the upwelling season is almost year-round at 30°375° (Figure 8, panel b).
752 At 40°375N, it shows almost perfect agreement between the data sources for season length and start time, with no clear temporal trend but with a large interannual variability. Values of up to 3
754 and 5 months year to year difference for start and duration, respectively, which can be related to the combined influence of large scale climate signals. Good agreement between wind products is
756 found for TUMI at 40.375°N although the CCMP is significantly lower, with a near-decadal modulation showing an increase in TUMI during the negative phase of the PDO associated with
758 high TUMI maxima in 2002, 2008 and 2013. There is a clear positive trend, which is assessed using the non-parametric SKTT method and the Matlab parametric "robustfit" function. The latter
760 performs an iterative least-squares regression to a linear model by iteratively changing the model

coefficients to limit the influence of the data points farthest from the linear model. For example, the "robusfit" linear regression gives less weight than a simple linear regression to the 1998/1999 TUMI data strongly affected by the 1998/1999 La Niña event (Figure 9, top panel). The use of "robustfit" gives a significant increase in TUMI between 1996 and 2018 of +27.2% (p=0.0655), +24.0% (p=0.0943), +15.2% (p= 0.1786), and +13.1% (p=0.2466) for CCMP, CMEMS, ERAI and ERA5, respectively. The use of SKTT gives +34.1% (p=0.039); +28.9% (p=0.051); +10.2% (p=0.342); +15.4% (p=0.09) for CCMP, CMEMS, ERAI and ERA5, respectively. Estimated trends with $p < 0.1$ are found only for CCMP and CMEMS, and these results are consistent with those obtained in section 4 although, not surprisingly, p-values vary.

At 30°375N, there are large differences in mean TUMI values, with CMEMS and ERAI being significantly lower, and the intriguing temporal evolution of the ERA5 data is again clearly indicated by much higher TUMI values at the beginning of the period. Although it does not vary as much as observed at 40°375N, due to the lack of strong seasonality, the low-frequency modulation shows periods of high TUMI, in 1998-1999 and 2010-2012, associated with negative phases of the PDO and ENSO. Over the period 1996-2018, the "robustfit" analysis gives a positive trend of +5.4% (p=0.3384), +5.7% (p=0.1728), and a negative trend of -29.5% (p= 0.0041) and -22.9% (p=0.0013) for CCMP, CMEMS, ERAI and ERA5, respectively. Using SKTT one obtains +3.1% (p=0.398); +1.3% (p=0.792); -21.6% (p=0.035); -26.2% (p=0.001) for CCMP, CMEMS, ERAI and ERA5, respectively. Only the estimated trends for ERAI and ERA5 exhibit a $p < 0.1$, which is consistent with the results of section 4. But it is still unexplained why the variability patterns in ERA5 are so different there, as well as the rapid increase in ERAI TUMI at the end of the period.

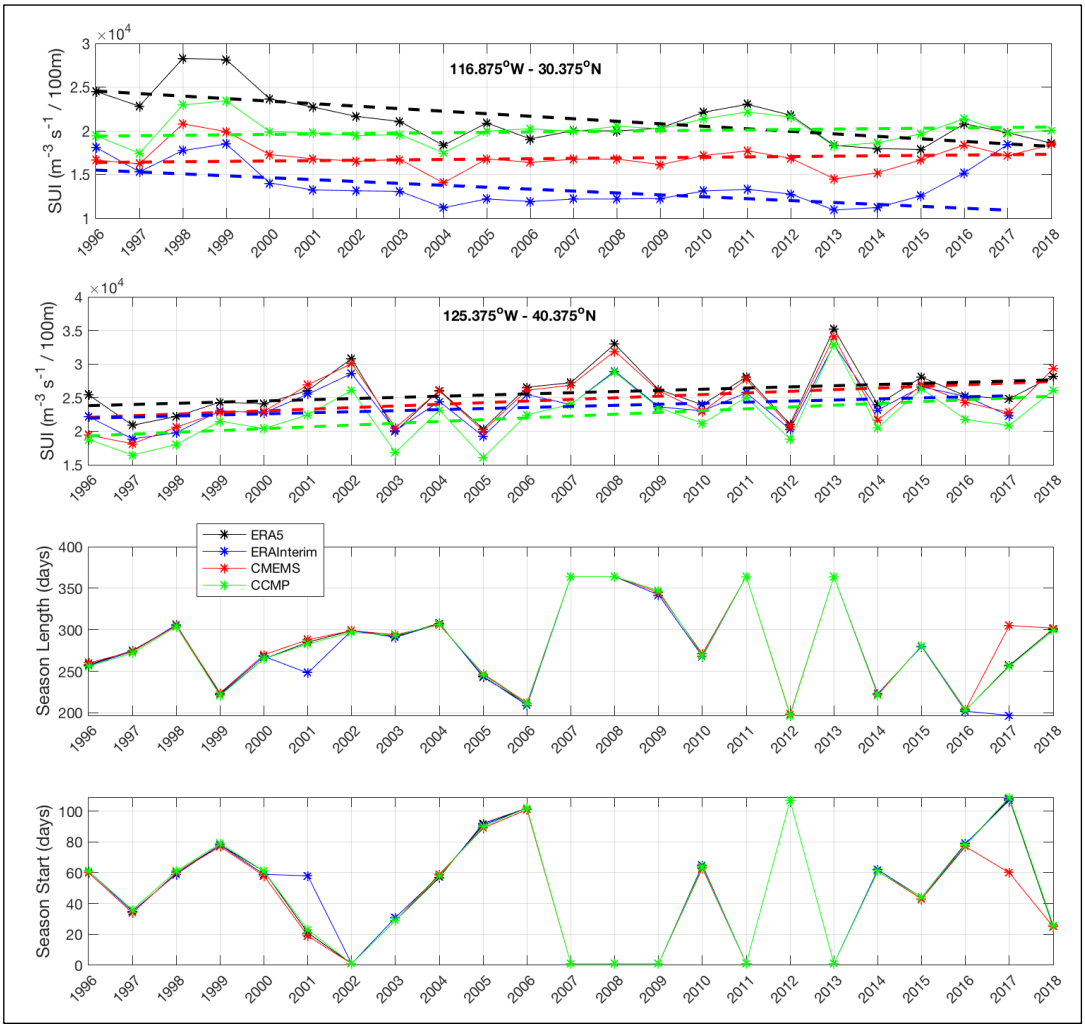

Figure 9. *Total Upwelling Magnitude Index (TUMI, $m^{-3}.s^{-1}$ per 100m) as a function of time at 116°875W – 30°375N, first top panel, and 125°375W – 40°375N, second top panel. For 125°375W – 40.375°N the associated upwelling season length (number of days, first lower panel), and day of upwelling season start in each year (second lower panel). Dashed lines in top panels show the trends obtained with the SKTT method. The color code follows ERA5 in black, ERAI in blue, CMEMS in red, CCMP in green.*

6. Discussion and summary

Long-term trends have been predicted in the four eastern boundary upwelling systems that are related to anthropogenic, deterministic and predictable changes in large-scale atmospheric pressure systems (Bakun, 1990; Bakun, 2015; Rykaczewski et al., 2015). In this work, we have examined the case of the California Current Upwelling System for the recent time period and have paid particular attention to the issue of data.

6.1 Surface wind data issues

Our approach is based on the use of surface winds from recent and mostly used model re-analyses (ERAI and ERA5) and satellite analyses (CCMP and CMEMS), over a period for which scatterometer wind vectors provide a reliable spatially-resolved dataset (speed and direction) and for which no large trends are observed in the most important climate signals in the Pacific Ocean. Therefore, although the 1996-2018 analysis period is relatively short with respect to natural near-decadal climate variability, a robust analysis of temporal trend can still provide reliable information on changes in upwelling winds over this period. Although the length of data records has been an obvious problem addressed in most studies of upwelling trends, a much overlooked issue is the long-term temporal consistency of the most widely used wind data sets.

In this regard, the use in our study of several different data sets with a discussion of their respective potential weaknesses is a necessary step. None of these data sets can be considered independent of the others, and each of them is likely to have uncharacterized biases that can be misinterpreted as geophysical trends. Indeed, although each of the wind products used in the study was developed with the objective of ensuring temporal consistency, this consistency is poorly documented and

830 therefore possibly unverified regionally. With respect to satellite data, the development of climate data records for each instrument is a recent concern and it can be therefore be difficult for multi-
832 satellite gridded products to achieve the accuracy required for climate studies (Bourassa et al., 2019). This may be due to problems related to the evolution of the observing systems and to the
834 difficulty to cross-calibrate the various instruments. But also due to the fact that the two main multi-satellite winds products (CCMP and CMEMS) both make use of ERAI model winds to ensure
836 consistency of analysis in satellite data gaps. The relative influence of ERAI winds in CMEMS products was extensively discussed in Desbiolles et al. (2017), using sensitivity experiments to
838 various input data, and validation using independent buoy and scatterometer data. They show a significant improvement in validation statistics for CMEMS winds compared to ERAI winds, but
840 they also conclude that the use of ERAI winds in CMEMS products may remain an obvious drawback. This supports our choice of a period for which scatterometer data are available with
842 good enough coverage to limit the influence of ERAI winds. For the numerical model winds, the surface winds from the 4-D model reanalysis are likely to be affected by several possible biases
844 other than that related to the calibration and editing of assimilated ocean surface wind data. As stated in Hersbach et al. (2018), spurious climate signals can be introduced from interaction
846 between atmospheric numerical model bias and the evolving observing system which remains a major concern in climate reanalysis. Any bias in the system can propagate and affect surface winds
848 through the 4D variational analysis. For example, Belmonte and Stoffelen (2019) showed systematic biases of several ms^{-1} in the ERAI and ERA5 winds relative to the ASCAT
850 scatterometer observations, with a strong dependence on latitude. Analyzing several atmospheric re-analyses, including the ERAI, with the CCMP as a baseline for comparison, Taboada et al.
852 (2019) showed similar results and concluded with a recommendation of testing the sensitivity of

derived results to the choice of wind product. This is what we have done to analyze trends in the CCUS, using the latest ERA5 and CMEMS products to help better mitigate the various data issues discussed in this section. Indeed, the ERA5 re-analysis is the ERAI follow-on and shows a great improvement over the latter data set at global and local scale (Hersbach et al., 2018; Hersbach et al., 2020; Belmonte and Stoffelen, 2019). Although we also show this significant improvement with the most recent re-analysis, large systematic, latitude-dependent biases between numerical and satellite upwelling winds still remain. ERA5 has generally larger upwelling wind magnitude and variability than CCMP and CMEMS during the first half of the period and closer statistics during the second half. The significant decrease in ERA5 upwelling winds over the period in the southern CCUS is not observed in satellite winds, which remains unexplained, indicating that large uncertainties, at the regional or global scale, can still remain in the most recent wind data sets (i.e. both model re-analyses and from satellites). The CMEMS data set shares many similar characteristics with the CCMP, but it has also different characteristics of interest for our analysis: 1) it does not use the buoy data which is done to allow independent assessment with these reference in-situ winds, and to avoid artifacts in the calculation of wind stress curl at locations close to buoys (Mears et al., 2019); 2) it is less dependent on ERAI numerical winds for our analysis period and in near-coastal areas because it uses a longer scatterometer data record and because it is not as constrained by ERAI winds over land as the CCMP is. Indeed, near the coast, the 25-50 km blind zone for satellite winds makes the CCMP winds (wind stress vector and curl) more strongly influenced by ERAI land winds, since CCMP also calculates winds over land. In coastal regions, the contamination of numerical model winds with lower winds over land and the coarse representation of the ocean-land transition in atmospheric reanalyses indeed degrade the ability to reproduce realistic upwelling patterns. In the methodological approach chosen for this study, we

876 therefore do not use the wind data for the grid pixels closest to the coast so that our results are less affected by these problems. Interestingly, at the offshore stations we have selected, we found a
878 remarkable agreement between CCMP and CMEMS upwelling winds and estimated trends. This may imply increased robustness in our results derived from wind analyses that are tailored to
880 satellite observations.

882 **6. 2 Observed trends in upwelling wind forcing and ecosystem response**

As we have consistently found for key biogeochemical system parameters (i.e. Chl-a, pCO_2 and
884 pH in our study) a spatially structured pattern of trends is observed in upwelling winds and associated Ekman transport with the four wind data sources, with trends towards more favorable
886 upwelling winds in the CCUS core (approximately between Point Conception to Cape Blanco, 35°-43° latitude). This trend is verified with $p < 0.1$ in the annual data only for the CCMP and CMEMS
888 satellite analyses. By defining seasons following the methods of García-Reyes and Largier (2012), seasonal trends of greater amplitude than the annual trend are identified, with $p < 0.1$, with a
890 comparable amplitude for model reanalysis and satellite analysis products in the winter (December-February) and upwelling (April-June) seasons. The relaxation season, from July to September, does
892 not show such a trend towards increased upwelling winds. Ambiguous results are found in the southern CCUS with negative trends found ($p < 0.1$) for the model reanalysis products but not from
894 the satellite products. This difference in trends is the result of the temporal evolution of geographically distributed average biases between the satellite analysis and the model reanalysis
896 products, which remain unresolved.

The strong spatial structuring of the observed trends for the biogeochemical parameters, pCO_2, pH
898 and Chl-a is consistent with long-term changes in upwelling modulating the carbonate system, as

discussed in Turi et al. (2016). Our results showing spatial structuring in the long-term trends of upwelling winds may explain the similar structuring observed in the increase in nearshore pCO_2 and Chl-a and decrease in pH, north of 34°N in the core of vthe CCUS. However, the precise relationships between the biogeochemical system of the CCUS and local or remote forcing can certainly be better analyzed by approaches that combine eddy-resolving regional models with various hydrographic and remote sensing observations (e.g. Jacox et al., 2016; Deutsch et al., 2020).

Previous studies devoted to the variability of the CCUS (e.g. García-Reyes and Largier, 2012; Sydeman et al., 2014) defined the upwelling season in a fixed time window, which raises the question of taking into account the large changes that occur in the upwelling phenology under natural climate forcing. Our results also show the large differences that occur in the timing of the upwelling season in response to the relative influence of the ENSO, NGPO and PDO, and this is consistent with previous studies (e.g. Di Lorenzo et al., 2008; Bograd et al., 2009; García-Reyes and Largier, 2012; Meinvielle and Johnson, 2013). The Cumulative Upwelling Index, CUI, is used to define the start and end times of the upwelling season and an associated seasonal upwelling index, the TUMI, represents the integration of the Ekman transport along the actual upwelling season. Variations in TUMI are better related to actual ocean productivity than an index calculated over a fixed time window to define the upwelling season. Changes in the timing of the upwelling season are remarkably consistent for satellite analyses and model re-analyses, but mean values of the TUMI vary significantly due to the observed differences in the mean along-shore wind stress between the different products. ERA5 TUMI values are significantly higher at the beginning of the period, resulting in differences in estimated trends. As observed throughout this study, there is remarkable agreement between the results obtained with the two satellite analysis data sets.

922 Remarkably, the satellite product results show that TUMI has increased by 25% or more in the central CCUS, whereas the model reanalyses give an increase of 15% or less. In the southern
924 CCUS, TUMI trends are negligible with satellite products, whereas a decrease in TUMI of 20% or more is achieved locally with model reanalysis products.

926

6.3 Summary

928 Long-term changes in the marine ecosystems of the EBUS are predicted due to anthropogenic climate change. In particular, global ocean acidification is having a profound effect on the coastal
930 waters of the EBUS, affecting the entire trophic chain, net primary production and related economic activities such as fisheries. Another predicted change related to human activity is that of upwelling
932 dynamics with expected long-term changes in upwelling winds, which raises the interest in monitoring upwelling using validated, self-consistent wind data sets. Indeed, the results of past
934 trend analyses using historical wind data show a high degree of uncertainty depending on the EBUS considered, the effect of natural climate fluctuations, the choice of wind dataset, the time period
936 considered, and the methodologies and significance tests applied. The California Current Upwelling System (CCUS) is already heavily impacted by major emerging climate trends such as
938 hypoxia and acidification, and strong remote forcing by natural climate fluctuations dominates near-decadal-scale wind trends and the associated ecosystem response. Therefore, the predicted
940 human-induced long-term trend in upwelling winds, regardless of when it may occur, is and will be difficult to assess if these issues listed are not properly addressed. We thus conducted a
942 sensitivity study on the use of surface winds from recent model re-analyses and satellite analyses, using a choice of the period 1996-2018 for which satellite winds provide a reliable spatially-
944 resolved wind dataset (both in speed and direction) and corresponding to a relatively neutral phase

of the most important climate signals in the Pacific Ocean. In particular, we intend to highlight the essential role that satellite measurements can play as a reliable source of baseline data for the ongoing monitoring of the CCUS.

Over the period 1996-2018, which shows start end years not associated with particular phases of PDO, NPGO or ENSO, there is a trend of increasing upwelling-favorable winds in the core of the CCUS (approximately between Point Conception and Cape Blanco), obtained with the different datasets and methodologies used, and conflicting results are found in the southern CCUS between the satellite and model products. In the core of the CCUS, there is also good agreement on stronger equatorward winds for the winter and spring seasons between the different datasets. Increase in upwelling favorable winds in the CCUS core is associated with a local increase of more than 25% in the seasonal upwelling transport index, as found with satellite products. The observed spatial structuring of the estimated wind trends is consistent with the trend analysis of water chlorophyll-a, partial pressure of CO_2, and basity (pH) analysis products.

However, systematic and time-dependent differences are found between the wind products, highlighting the need to further investigate the poorly documented temporal stability of these widely used wind climatology products. More sustained efforts are therefore needed to fully understand the differences between the analyzed datasets, some of which are likely due to artificial (non-physical) non-stationarity behavior or to systematic regional differences.

Acknowledgments

This study was conducted as part of the OceanSODA project, funded by the European Space Agency under the contract 4000112091/14/I-LG. The authors thank Antoine Grouazel for the production of the upwelling indices products, and the reviewers who helped to improve the manuscript.

References

Atlas, R., Hoffman, R.N., Ardizzone, J., Leidner, S.M., Jusem, J.C., Smith, D.K., Gombos, D., 2011. A cross-calibrated, multiplatform ocean surface wind velocity product for meteorological and oceanographic applications, *B. Amer. Meteorol. Soc.,* **92**, 157–174.

Bakun, A., 1973. Coastal upwelling indices, West Coast of North America, 1946–71. US Department of Commerce, National Oceanic and Atmospheric Administration, National Marine Fisheries Service.

Bakun, A., 1990. Global climate change and intensification of coastal ocean upwelling, *Science*, **247**, 198–201.

Bakun, A., Black, B.A., Bograd, S.J., et al., 2015. Anticipated Effects of Climate Change on Coastal Upwelling Ecosystems. *Curr. Clim. Change Rep.,* **1,** 85–93. https://doi.org/10.1007/s40641-015-0008-4.

Belmonte Rivas, M., Stoffelen, A., 2019. Characterizing ERA-interim and ERA5 surface wind biases using ASCAT. *Ocean Sci*. ,**15**. https://doi.org/10.5194/os-15-831-2019.

Bentamy, A., Croize-Fillon, D., 2012. Gridded surface wind fields from Metop/ASCAT measurements. *Int. J. Remote Sens.*, **33**, 1729-1754. DOI 10.1080/01431161.2011.600348.

Bograd, S. J. et al., 2009. Phenology of coastal upwelling in the California Current. *Geophys. Res. Lett.,* **36**, L01602.

Bonino, G., Di Lorenzo, E., Masina, S., et al., 2019. Interannual to decadal variability within and across the major Eastern Boundary Upwelling Systems. *Sci. Rep.,* **9,** 19949. https://doi.org/10.1038/s41598-019-56514-8.

Bourassa, M., Meissner, T., Cerovecki, I., Chang, P., Dong, X., De Chiara, G., et al., 2019. Remotely sensed winds and wind stresses for marine forecasting and ocean modeling. *Front. Mar. Sci.,* **9**. https://doi:10.3389/fmars.2019.00443.

Brady, R. X., Alexander, M. A., Lovenduski, N. S., & Rykaczewski, R. R., 2017. Emergent anthropogenic trends in California Current upwelling. *Geophy. Res. Lett*., **44**, 5044-5052.

Capet, X.J., Marchesiello, P., McWilliams, J.C., 2004. Upwelling response to coastal wind profiles. *Geophys. Res. Lett*., **31**, L13311. https://doi:10.1029/ 2004GL020123.

1014 Carvalho, D., Rocha, A., Gómez-Gesteira, M., Silva Santos, C., 2014. Comparison of reanalyzed, analyzed, satellite-retrieved and NWP modelled winds with buoy data along the Iberian Peninsula
1016 coast. *Remote Sens. Environ.*, **152**, 480–492.

1018 Chan, F., Barth, J.A., Blanchette, C.A., et al., 2017. Persistent spatial structuring of coastal ocean acidification in the California Current System. *Sci. Rep*., **7**, 2526. https://doi.org/10.1038/s41598-
1020 017-02777-y.

1022 Chau, T.T.T., Gehlen, M., Chevallier, F., 2020. Quality Information Document for Global Ocean Surface Carbon Product MULTIOBS_GLO_BIO_CARBON_SURFACE_REP_015_008. CMEMS-
1024 MOB-QUID-015-008, https://resources.marine.copernicus.eu/documents/QUID/CMEMS-MOB-QUID-015-008.pdf/ (accessed 19 April 2021).

1026

Chavez, F.P., Pennington, J.T., Michisaki, R.P., Blum, M., Chavez, G.M., Friederich, J.,
1028 Jones, B., Herlien, R., Kieft, B., Hobson, B., Ren, A.S., Ryan, J., Sevadjian, J.C., Wahl, C., Walz, K.R., Yamahara, K., Friederich, G.E., Messié, M., 2017. Climate variability and
1030 change: Response of a coastal ocean ecosystem. *Oceanography,* **30(4)**, 128–145. https://doi.org/10.5670/oceanog.2017.429.

1032

Chelton, D., Xie, S.P., 2010. Coupled ocean-atmosphere interactions at oceanic mesoscales,
1034 *Oceanography*, **23**, 52–69.

1036 Chenillat, F., Rivière, P., Capet, X., Di Lorenzo, E., Blanke, B., 2012. North Pacific Gyre Oscillation modulates seasonal timing and ecosystem functioning in the California Current
1038 upwelling system. *Geophys. Res. Lett.,* **39**, L01606.

1040 Dee, D., and Coauthors, 2011. The ERA-Interim reanalysis: Configuration and performance of the data assimilation system. *Quart. J. Roy. Meteor. Soc*., **137**, 553–597.

1042

Denvil-Sommer A., Gehlen, M., Vrac, M., Mejia, C., 2019. LSCE-FFNN-v1: the reconstruction of
1044 surface ocean pCO_2. *Geosc. Model Dev.*, **12**, pp.2091-2105.

1046 Desbiolles, F. et al., 2017. Two decades [1992–2012] of surface wind analyses based on satellite scatterometer observations. *J. of Mar. Sys.*, **168**. https://doi.org/10.1016/j.jmarsys.2017.01.003.

1048

Deutsch, C., Frenzel, H., McWilliams, J.C., Renault, L., Kessouri, F., Howard, Liang, J.H.,
1050 Bianchi, D., 2020. Biogeochemical variability in the California Current System., *Progr. Oceanogr.* https://doi.org/10.1101/2020.02.10.942565 , in press.

1052

Di Lorenzo, E. and Coauthors, 2008. North Pacific Gyre Oscillation links ocean climate and
1054 ecosystem change. *Geophys. Res. Lett.,* **35**, L08607. https://doi.org/10.1029/2007GL032838.

1056 Di Lorenzo, E., 2015. The future of coastal ocean upwelling. *Nature,* **518,** 310–311. https://doi.org/10.1038/518310a.

1058

Ding, H., Alexander, M. A., Jacox, M. G., 2021. Role of geostrophic currents in future changes of coastal upwelling in the California Current System. *Geophys. Res. Lett*., **48**, e2020GL090768. https://doi.org/10.1029/2020GL090768.

Ekman, V.W., 1905. On the infuence of the earth's rotation on ocean-currents. *Arkiv for Matematik, Astronomy och Fysik* **2(11)**. https://jscholarship.library.jhu.edu/bitstream/handle/1774.2/33989/31151027498728.pdf?sequences=80&isAllowed=y (accessed 19 April 2021)

Estrade, P., Marchesiello, P., De Verdière, A.C., Roy, C., 2008. Cross-shelf structure of coastal upwelling : a two – dimensional extension of Ekman's theory and a mechanism for inner shelf upwelling shut down. *J. Mar. Res*., **66**, http://dx.doi.org/10.1357/002224008787536790.

Feely, R.A., Sabine, C.L., Hernandez-Ayon, J.M., Ianson, D., Hales, B., 2008. Evidence for upwelling of corrosive "acidified" water onto the continental shelf. *Science,* **320**, 1490–1492. https://doi: 10.1126/science.1155676.

García-Reyes, M., Largier, J., 2010. Observations of increased wind-driven coastal upwelling off central California, *J. Geophys. Res*., **115**. https://doi:10.1029/2009JC005576.

García-Reyes, M., Largier, J., 2012. Seasonality of coastal upwelling off central and northern California: New insights, including temporal and spatial variability, *J. Geophys. Res.*, **117**. https://doi:10.1029/2011JC007629.

García-Reyes, M., Sydeman, W. J., Schoeman, D. S., Rykaczewski, R. R., Black, B. A., Smit, A. J., Bograd, S. J., 2015. Under pressure: Climate change, upwelling and eastern boundary upwelling ecosystems. *Front. Mar. Sci.*, **2**. https://doi.org/10.3389/fmars.2015.00109.

Gruber, N., Hauri, C., Lachkar, Z., Loher, D., Fr¨olicher, T. L., Plattner, G.-K., 2012. Rapid progression of ocean acidification in the California Current System. *Science*, **337**, 220–223.

Halpern, D., 2002. Offshore Ekman transport and Ekman pumping off Peru during the 1997–1998 El Niño. *Geophys. Res. Lett*., **29.** https://doi:10.1029/2001GL014097.

Hauri, C., Gruber, N., Vogt, M., Doney, S.C., Feely, R.A., Lachkar, Z., Leinweber, A., McDonnell, A.M.P., Munnich, M., Plattner, G.K., 2013. Spatiotemporal variability and long-term trends of ocean acidification in the California Current System. *Biogeosci*., **10**, 193–216. https://doi:10.5194/bg-10-193-2013.

Hersbach, H. , 2011. Sea-surface roughness and drag coefficient as function of neutral wind speed. *J. Phys. Oceanogr*., **41**, 247–251.

Hersbach, H., and Coauthors, 2018. Operational global reanalysis: progress, future directions and synergies with NWP. *ECMWF Report Series,* **27**, ECMWF, Reading, UK.

Hersbach, H., and Coauthors, 2020. The ERA5 global reanalysis. *Quarterly Journal of the Royal Meteorological Society*, **146**, 1– 51. https://doi.org/10.1002/qj.3803.

1106 Hirsch, R. M., Slack, J. R., and Smith, R. A., 1982. Techniques of trend analysis for monthly water quality data, *Water Resour. Res*., **18**,107–121. https://doi.org/10.1029/WR018i001p00107.

1108

Hirsch, R.M., Slack, J.R., 1984. A non-parametric trend test for seasonal data with serial 1110 dependence, *Water Resour. Res*., **20**, 727 732. https://doi.org/10.1029/WR020i006p00727.

1112 Iles, A. C. et al., 2012. Climate-driven trends and ecological implications of event-scale upwelling in the California Current System. *Glob. Change Biol.,* **18**, 783–796.

1114

Jacox, M. G., Moore, A. M., Edwards, C. A., Fiechter, J., 2014. Spatially resolved upwelling in the 1116 California Current System and its connections to climate variability. *Geophys. Res. Lett.,* **41**, 3189–3196.

1118

Jacox, M. G., Bograd, S. J., Hazen, E. L., & Fiechter, J., 2015. Sensitivity of the California Current 1120 nutrient supply to wind, heat, and remote ocean forcing. *Geophys. Res. Lett*., **42**, 5950-5957.

1122 Jacox, M. G., Hazen, E. L., & Bograd, S. J., 2016. Optimal environmental conditions and anomalous ecosystem responses: Constraining bottom-up controls of phytoplankton biomass in the 1124 California Current System. *Scientific reports*, **6**, 27612.

1126 Jacox, M. G., Edwards, C.A., Hazen, E.L., Bograd, S.J., 2018. Coastal upwelling revisited, Ekman, Bakun, and improved upwelling indices for the U.S. West Coast. *J. Geophys. Res.*, **123**. 1128 https://doi.org/10.1029/2018JC014187.

1130 Jackson, T., and co-authors, 2019. Ocean Colour Climate Change Initiative. *Product user guide D3.4PUG*. https://climate.esa.int/en/projects/ocean-colour/key-documents/ (accessed 19 April 1132 2021).

1134 Kahru, M., Jacox, M. G., & Ohman, M. D., 2018. CCE1: decrease in the frequency of oceanic fronts and surface chlorophyll concentration in the California Current System during the 2014- 1136 2016 northeast Pacific warm anomalies. *Deep Sea Research Part I: Oceanographic Research Papers*, **140**, 4-13.

1138

Kent, E. C., Fangohr, S., and Berry, D. I., 2013. A comparative assessment of monthly mean wind 1140 speed products over the global ocean. *Inter. J. Climatol.* **33**, 2520–2541. https://doi: 10.1002/joc.3606.

1142

Lachkar, Z., 2014. Effects of upwelling increase on ocean acidification in the California and 1144 Canary Current Systems. *Geophys. Res. Lett*., **41**. https://doi:10.1002/2013GL058726.

1146 Land, P.E., Shutler, J.D., Findlay, H.S., Girard-Ardhuin, F., Sabia, R., Reul, N., Piolle, J.-F., Chapron, B., Quilfen, Y., et al., 2015. Salinity from space unlocks satellite-based assessment of 1148 ocean acidification. *Environ. Sci. Tech*. **49**, 987–1,994, http://dx.doi.org/ 10.1021/es504849s.

1150 Land, P.E., Findlay, H.S., Shutler, J.D., Ashton, I., Holding, T., Grouazel, A., Ardhuin, F., Reul, N., Piolle, J.-F., Chapron, B., Quilfen, Y., et al., 2019. Optimum satellite remote sensing of the
1152 marine carbonate system using empirical algorithms in the global ocean, the Greater Caribbean, the Amazon Plume and the Bay of Bengal**.** *Remote Sens. Environ*., **235**.
1154 https://doi :10.1016/j.rse.2019.111469.

1156 Marchesiello, P., Estrade, P., 2010. Upwelling limitation by onshore geostrophic flow. *J. Mar. Res*., **68**, p. 37-62. ISSN 0022-2402.
1158

Mears, C. A., Scott, J., Wentz, F. J., Ricciardulli, L., Leidner, S. M., Hoffman, R., Atlas, R., 2019.
1160 A Near-Real-Time Version of the Cross-Calibrated Multiplatform (CCMP) Ocean Surface Wind Velocity Dataset. *J. Geophys. Res*., **124**. https://doi.org/10.1029/2019JC015367.
1162

Meinvielle, M.**,** Johnson, G.C**.,** 2013**.** Decadal water-property trends in the California
1164 Undercurrent, with implications for ocean acidification. *J. Geophys. Res. Oceans,* **118**, 6687–703.

1166 Narayan, N., Paul, A., Mulitza, S., Schulz, M., 2010. Trends in coastal upwelling intensity during the late 20th century. *Ocean Sci.* **6**, 815–823.
1168

Pickett, M. H., Paduan, J.D., 2003. Ekman transport and pumping in the California Current based
1170 on the U.S. Navy's high-resolution atmospheric model (COAMPS). *J. Geophys. Res.*, **108**. https://doi:10.1029/2003JC001902.

1172 Quilfen, Y., Chapron, B., Vandemark, D., 2001. The ERS scatterometer wind measurement accuracy: Evidence of seasonal and regional biases. *J. Atmos. Ocean. Tech.*, **18**, 1684-1697. 1174 https://doi.org/10.1175/1520-0426(2001)018<1684:TESWMA>2.0.CO;2.

1176 Quilfen, Y., Chapron, B., Collard, F., Vandemark, D., 2004. Relationship between ERS scatterometer measurement and integrated wind and wave parameters. *J. Atmos. Ocean. Tech*, **21**, 1178 368-373. https://doi.org/10.1175/1520-0426(2004)021<0368:RBESMA>2.0.CO;2.

1180 Renault, L., Hall, A., McWilliams, J.C., 2015. Orographic shaping of U.S. West Coast wind profiles during the upwelling season. *Climate Dyn.*, **46**, 273–289. https://doi.org/10.1007/s00382-1182 015-2583-4.

1184 Renault, L., Deutsch, C., McWilliams, J.C., 2016. Partial decoupling of primary productivity from upwelling in the California Current system. *Nature Geosc.,* **9,** 505–508. 1186 https://doi.org/10.1038/ngeo2722.

1188 Rykaczewski, R.R., Checkley, D.M., 2008. Influence of ocean winds on the pelagic ecosystem in upwelling regions. *Proc. Natl. Acad. Sci.,* **105**, 1965–70.

1190

Rykaczewski, R.R., Dunne, J.P., Sydeman, W.J., García-Reyes, M., Black, B.A., Bograd, S.J., 1192 2015. Poleward displacement of coastal upwelling-favorable winds in the ocean's eastern boundary currents through the 21st century, *Geophys. Res. Lett*., **42**, 6424–6431. 1194 https://doi:10.1002/2015GL064694.

1196 Sen, P. K., 1968. Estimates of the regression coefficient based on Kendal's Tau. *J. Am. Stat. Assoc.,* **63**, 1379–1389. https://doi:10.1080/01621459.1968.10480934.

1198

Serinaldi, F., Kilsby, C.G., Lombardo, F., 2018. Untenable non-stationarity: An assessment of the

1200 fitness for purpose of trend tests in hydrology. *Adv. Water Resour.*, **111**, 132-155. https://doi.org/10.1016/j.advwatres.2017.10.015.

1202

Shutler, J.D., Wanninkhof, R., Nightingale, P.D., Woolf, D.K., Bakker, D.C.E., Watson, A.,

1204 Ashton, I., Holding, T., Chapron, B., Quilfen, Y., et al., 2019. Satellites will address critical science priorities for quantifying ocean carbon. *Front. Ecol. Environ.*, **18**, 27-35.

1206

Sydeman, W. J. et al., 2014. Climate change and wind intensification in coastal upwelling

1208 ecosystems. *Science,* **345**, 77–80.

1210 Taboada, F. G., Stock, C. A., Griffies, S. M., Dunne, J., John, J. G., Small, R. J., & Tsujino, H., 2019. Surface winds from atmospheric reanalysis lead to contrasting oceanic forcing and coastal

1212 upwelling patterns. *Ocean Modelling*, **133**, 79-111.

1214 Turi, G., Lachkar, Z., Gruber, N., Münnich, M., 2016. Climatic modulation of recent trends in ocean acidification in the California Current System. *Envir. Res. Lett.,* **11**, 014007.

1216

Young, I. R., Ribal, A., 2019. Multiplatform evaluation of global trends in wind speed and wave height. *Science,* **364**, 548–552.

Wang, D., Gouhier, T., Menge, B. *et al.*, 2015. Intensification and spatial homogenization of coastal upwelling under climate change. *Nature,* **518,** 390–394. https://doi.org/10.1038/nature14235

Wang, Y.H., Walter, R.K., White, C., Farr, H.K., Ruttenberg, B.I., 2019. Assessment of surface wind datasets for estimating offshore wind energy along the Central California Coast. *Renew. Energy*, **133**, 343-353. https://doi.org/10.1016/j.renene.2018.10.008

Appendix A

Table 1 : For the twelve stations, one by row, shown in Figure 2, from left to right column: station number, longitude (degree), latitude (degree), distance to coast (D2coast, km), seafloor depth (m), coast angle (degree, anticlockwise from the eastward axis).

Station number	Longitude (degrees)	Latitude (degrees)	D2coast (km)	Depth (m)	Coast angle (degrees)
1	-112.875	24.375	101	2827	122
2	-114.625	26.375	93	3476	138
3	-115.375	28.375	103	342	138
4	-116.875	30.375	81	2364	114
5	-119.125	32.375	178	343	142
6	-121.375	34.375	97	2454	125
7	-122.875	36.375	95	3140	104
8	-124.375	38.375	93	3730	124
9	-125.375	40.375	98	1807	92
10	-125.375	42.375	83	3078	93
11	-125.125	44.375	88	1099	82
12	-125.125	46.375	92	1592	109

1246

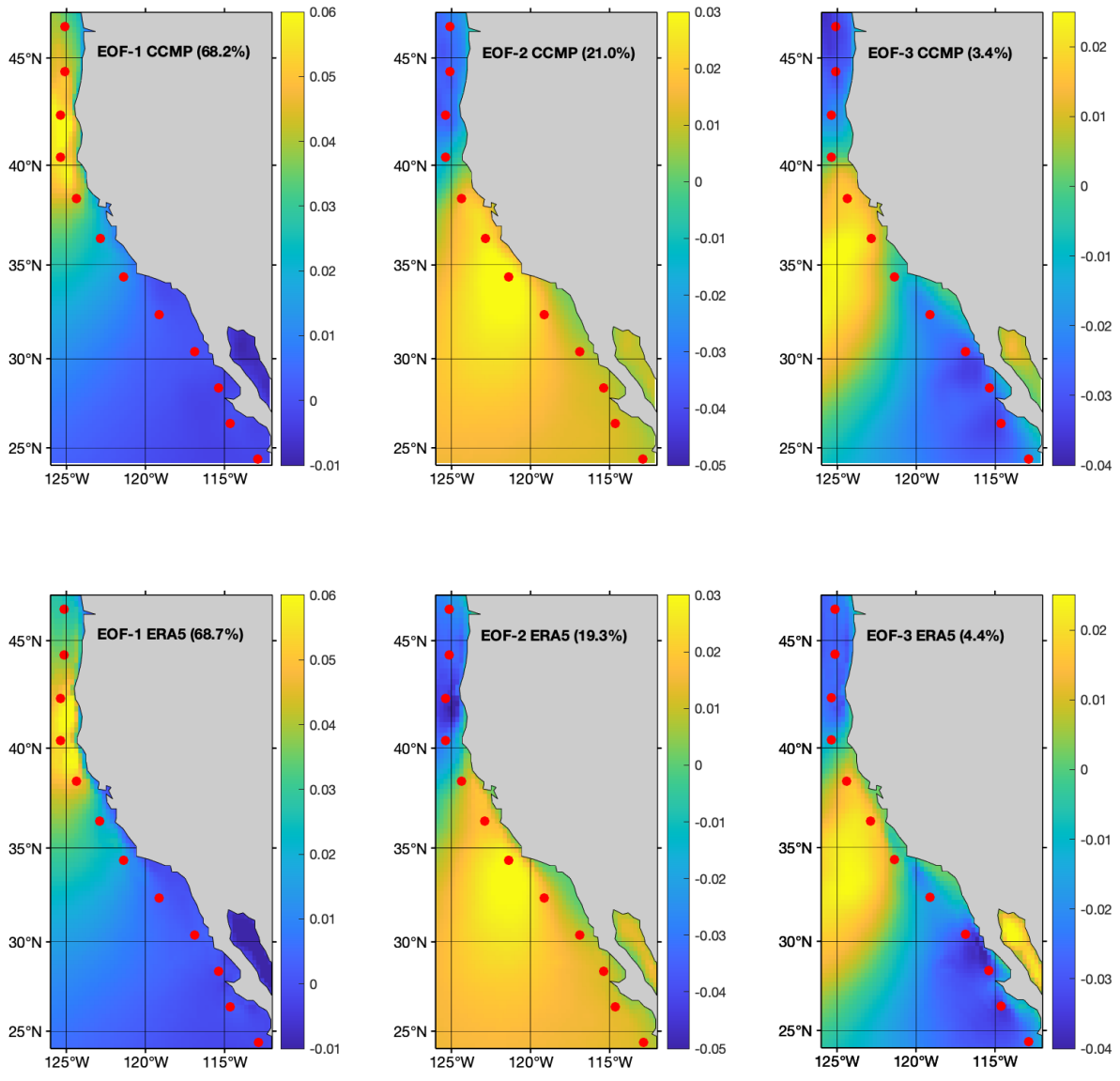

1248

Figure A1: First three EOFs of the meridional wind stress component for CCMP (top) and ERA5

1250 (bottom). Red dots give the location of the 12 stations. The percentage of variance accounted for by the first three EOFs is 68.7, 19.3, 4.4 for ERA5; 68.2, 21.0, 3.4 for CCMP.

1252

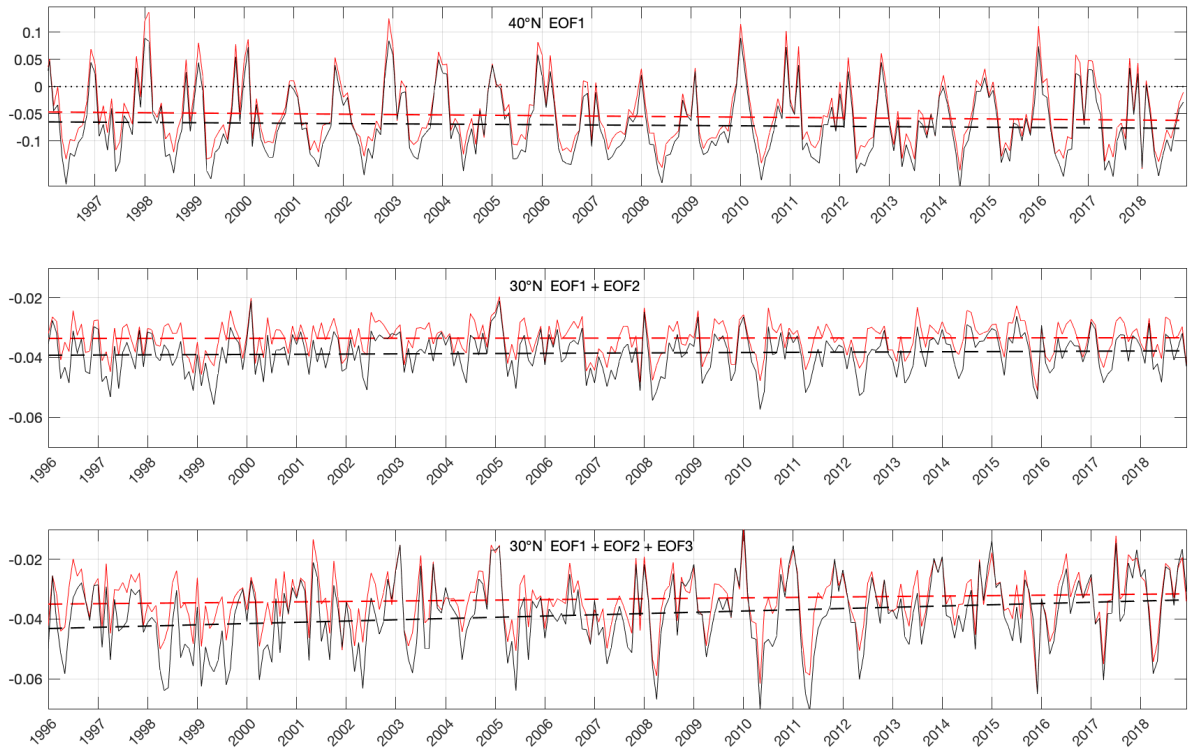

Figure A2: Time series at station 9 (40°N, top panel) and station 4 (30°N, center and bottom panels) of the meridional wind stress EOF components (N.m^{-2}, solid lines) and associated estimated trend lines (dashed lines) for CCMP (red) and ERA5 (black).

At 40°N, station 9 , the percentage of variance accounted for by EOF1 is 91.5% and 95.4% for ERA5 and CCMP, respectively.

At 30°N, station 4, the percentage of variance accounted for by the first three EOFs is 5.2, 21.0, 56.0 for ERA5 and 0.2, 27.6, 49.5 for CCMP. The meridional wind stress component is reconstructed with the two first EOFs (center panel), and with the three first EOFs (bottom panel). See section 2.2 for discussion.

List of Figures Captions

Figure 1. Taylor diagrams for comparison of CMEMS (left panels), ERAInterim (center panels), ERA5 (right panels) τ_{upw} with the CCMP data. The radial axis represents the normalized standard deviation (STD), with the unit value referenced as the CCMP STD; the root mean square differences (RMSD) with respect to the CCMPdata are represented by green dashed arcs and numbers (Nm^{-2}); the correlation coefficients vary in the azimuthal direction as blue dashed-dotted lines and numbers; and the diamonds are color-coded according to the mean bias with respect to the CCMP (Nm^{-2}). Top: 1996-2006; Bottom 2007-2018.

Figure 2. Location of the twelve stations (dots) and seafloor elevation (left, m), mean Ekman vertical velocity (center, ms^{-1}, zero-contour as a magenta solid line), and mean Ekman transport (right, m^2s^{-1}, black arrows indicate the orientation of the coastline used to derive τ_{upw})

Figure 3. Monthly values of climate indices: top, North Pacific Gyre Oscillation (NPGO) index, center, Pacific Decadal Oscillation (PDO) index, bottom, multivariate El Niño Southern Oscillation (ENSO) index.

Figure 4. top panel: trends in Chl-a ($mg\ m^{-3}\ yr^{-1}$) nearshore (distance to coast < 50 km, red solid line) and offshore (75 km < distance to coast < 150 km, blue solid line) for the period 1998-2018. Central and bottom panels: trends in pCO_2 (central panel, $0.1Pa\ yr^{-1}$) and pH (bottom panel) for the periods 1998-2018 (red solid line) and 1985-2018 (blue solid line). The colored areas correspond to a p-value < 0.1.

Figure 5. Monthly values of coastal Chl-a (mg m^{-3}, averaged over a distance to coast < 50 km) for the periods 1998-2018, and seasonal values such as: December/January/February (DJF, blue line), April/May/June (AMJ, green line), July/August/September (JAS, red line). March/October/November (MON, black line). The dashed black lines show the trend as estimated in Figure 4. The latitude shown in the upper left corner of each plot is the latitude of the coastal point located on the perpendicular to stations 1, 3, 5, 7, 9, 11 from bottom-right to top-left (see Table A1 for details).

Figure 6. Top panels: Annual τ_{upw} trends ($N.m^{-2}$ per year, negative for increasing equatorward winds) as a function of latitude, for the twelve stations, over the period 1996-2018, for model winds (left panel) and satellite winds (right panel).The color-shaded areas correspond to p-value < 0.1. Bottom panels: Seasonal τ_{upw} trends ($N.m^{-2}$ per year) over the same period and on the same x-axis for model winds (left panel) and satellite winds (right panel), for the winter season (solid lines), the upwelling season (dashed lines), and the transition season (dashed-dotted lines). Filled squares indicate $p < 0.1$. The color code follows ERA5 in black, ERAI in blue, CMEMS in red, CCMP in green.

Figure 7. Top panel: average integrated Ekman pumping transport (m^3s^{-1} per 100m of coast) as a function of latitude, for the twelve stations, averaged over the 1996-2018 period. Lower panel: associated trends (m^3s^{-1} per year) over the same period and same x-axis for ERA5 in black, CMEMS in red, CCMP in green.

1312 **Figure 8.** Mean alongshore upwelling winds (τ_{upw}, $N.m^{-2}$, negative when equatorward) and associated CUI ($m^{-3}.s^{-1}$ / 100m) as a function of time, at 116°875W – 30°375N (top panels) and
1314 125°375W – 40°375N (bottom panels). The color code follows ERA5 in black, CMEMS in red, CCMP in green, ERAInterim in blue.

1316

1318 **Figure 9.** Total Upwelling Magnitude Index (TUMI, $m^{-3}.s^{-1}$ per 100m) as a function of time at 116°875W – 30°375N, first top panel, and 125°375W – 40°375N, second top panel. For 125°375W
1320 – 40.375°N the associated upwelling season length (number of days, first lower panel), and day of upwelling season start in each year (second lower panel). Dashed lines in top panels show the
1322 trends obtained with the SKTT method. The color code follows ERA5 in black, ERAI in blue, CMEMS in red, CCMP in green.

1324

1326 **Figure A1.** First three EOFs of the meridional wind stress component for CCMP (top) and ERA5 (bottom). Red dots give the location of the 12 stations. The percentage of variance accounted for
1328 by the first three EOFs is 68.7, 19.3, 4.4 for ERA5; 68.2, 21.0, 3.4 for CCMP.

1330

Figure A2. Time series at station 9 (40°N, top panel) and station 4 (30°N, center and bottom panels)
1332 of the meridional wind stress EOF components ($N.m^{-2}$, solid lines) and associated estimated trend lines (dashed lines) for CCMP (red) and ERA5 (black).

1334 At 40°N, station 9 , the percentage of variance accounted for by EOF1 is 91.5% and 95.4% for ERA5 and CCMP, respectively.

1336 At 30°N, station 4, the percentage of variance accounted for by the first three EOFs is 5.2, 21.0, 56.0 for ERA5 and 0.2, 27.6, 49.5 for CCMP. The meridional wind stress component is

1338 reconstructed with the two first EOFs (center panel), and with the three first EOFs (bottom panel). See section 2.2 for discussion.

1340

1342